1 A full-coverage satellite-based global atmospheric CO₂ dataset at 0.05°

2 resolution from 2015 to 2021 for exploring global carbon dynamics

- 3 Zhige Wang^{1,2,3}, Ce Zhang^{4,5}, Kejian Shi⁶, Yulin Shangguan^{1,2}, Bifeng Hu^{7,8}, Xueyao Chen^{1,2,9}, Danqing
- Wei^{1,2,10}, Songchao Chen^{1,2,11*}, Peter M. Atkinson^{12,13}, Qiang Zhang³
- ¹ State Key Laboratory of Soil Pollution Control and Safety, Zhejiang University, Hangzhou, 310058,
- 6 China
- ⁷ College of Environmental and Resource Sciences, Zhejiang University, Hangzhou 310058, China
- 8 ³ Ministry of Education Key Laboratory for Earth System Modeling, Department of Earth System Science,
- 9 Tsinghua University, Beijing 100084, China
- 10 ⁴ School of Geographical Sciences, University of Bristol, Bristol BS8 1SS, UK
- 11 5 UK Centre for Ecology & Hydrology, Library Avenue, Bailrigg, Lancaster LA1 4AP, UK
- 12 ⁶ School of Geographical Sciences, Faculty of Science and Engineering, University of Nottingham
- 13 Ningbo China, Ningbo 315100, China
- 14 ⁷ Department of Land Resource Management, School of Public Administration, Jiangxi University of
- 15 Finance and Economics, Nanchang, 330013, China
- 16 ⁸Key Laboratory of Data Science in Finance and Economics of Jiangxi Province, Jiangxi University of
- 17 Finance and Economics, Nanchang, 330013, China
- 18 ⁹Department of Earth and Environmental Sciences, Faculty of Science, The Chinese University of Hong
- 19 Kong, Sha Tin, Hong Kong, China
- 20 ¹⁰ Zhejiang Economic Information Center, Hangzhou, 310006, China
- 21 II ZJU-Hangzhou Global Scientific and Technological Innovation Center, Zhejiang University, Hangzhou
- 22 311215, China
- 23 Lancaster Environment Centre, Lancaster University, Lancaster LAI 4YO, UK
- 24 ¹³ Geography and Environment, University of Southampton, Highfield, Southampton SO17 1BJ, UK

26

25

* Corresponding author: Songchao Chen (chensongchao@zju.edu.cn)

28 Abstract

The irreversible trend for global warming underscores the necessity for accurate
monitoring and analysis of atmospheric carbon dynamics on a global scale. Carbon
satellites hold significant potential for atmospheric CO2 monitoring. However, existing
studies on global CO_2 are constrained by coarse resolution (ranging from 0.25° to 2°)
and limited spatial coverage. In this study, we developed a new global dataset of
column-averaged dry-air mole fraction of CO_2 (XCO ₂) at 0.05° resolution with full
coverage using carbon satellite observations, multi-source satellite products, and an
improved deep learning model. We then investigated changes in global atmospheric
CO_2 and anomalies from 2015 to 2021. The reconstructed XCO_2 products show a better
agreement with Total Carbon Column Observing Network (TCCON) measurements,
with R ² of 0.92 and RMSE of 1.54 ppm. The products also provide more accurate
information on the global and regional spatial patterns of XCO2 compared to origin
carbon satellite monitoring and previous XCO_2 products. The global pattern of XCO_2
exhibited a distinct increasing trend with a growth rate of 2.32 ppm/year, reaching
414.00 ppm in 2021. Globally, XCO ₂ showed obvious spatial variability across
different latitudes and continents. Higher XCO2 concentrations were primarily
observed in the Northern Hemisphere, particularly in regions with intensive
anthropogenic activity, such as East Asia and North America. We also validated the
effectiveness of our XCO2 products in detecting intensive CO2 emission sources. The
XCO_2 dataset is publicly accessible on the Zenodo platform at
https://doi.org/10.5281/zenodo.12706142 (Wang et al., 2024a). Our products enable
enhanced ability in identifying regional- and county-level XCO2 hotpots, carbon
emissions and fragmented carbon sinks, providing a robust basis for targeted global
carbon governance policies.

- **Keywords:** Atmospheric carbon dioxide; Satellite carbon monitoring; Deep learning;
- 55 OCO-2/3

1. Introduction

Carbon dioxide (CO₂) is a primary greenhouse gas (GHG). Anthropogenic activities and land use change since the industrial revolution have led to a marked

increase in atmospheric CO₂, which is widely considered to be a major contributor to climate change, reaching a record-high of 414.71 parts per million (ppm) in 2021 (Friedlingstein et al., 2022). The damaging global climate change caused by atmospheric increases in CO₂ is severe and irreversible (IPCC, 2023; Kemp et al., 2022; Solomon et al., 2009). Consequently, the Paris Agreement announced to hold "the increase in the global average temperature to well below 2°C above pre-industrial levels" and pursue efforts "to limit the temperature increase to 1.5°C above pre-industrial levels." It was also determined that the joined parties should submit their nationally determined contributions (NDCs) to reduce CO₂ emissions.

60

61

62

63

64

65

66

67

68

69

70

71

72

73

74

75

76

77

78

79

80

81

82

83

84

85

86

87

88

89

90

91

92

93

Accurate monitoring of atmospheric CO₂ concentrations is crucial for measuring global CO₂ emissions mitigation as well as characterizing terrestrial carbon change. Currently, ground-based and airborne platform-based atmospheric CO₂ observation networks, such as the Total Carbon Column Observing Network (TCCON, https://tccondata.org/), are capable of providing CO₂ measurements with high accuracy (Petzold et al., 2016; Wunch et al., 2011, 2010). However, these observation networks are insufficient to fully explore the spatiotemporal patterns of atmospheric CO₂ at a global scale. The launch of a series of carbon observation satellites in recent years has provided favorable opportunities for continuous and large-scale atmospheric CO₂ observation (Buchwitz et al., 2015; Hammerling et al., 2012). The Scanning Imaging Absorption Spectrometer for Atmospheric Chartography (SCIAMACHY) onboard EnviSat was one of the first instruments to monitor the atmospheric column-averaged dry-air mole fraction of CO₂ (XCO₂) (Bovensmann et al., 1999). The Greenhouse Gases Observing Satellite (GOSAT) launched by Japan utilized the Thermal And Near-Infrared Sensor for carbon Observation (TANSO) instrument to monitor XCO₂ globally, providing products with a spatial resolution of 10 km every three days (Butz et al., 2011). The Orbiting Carbon Observatory-2 (OCO-2) and OCO-3 launched by NASA provide XCO₂ measurements at a finer spatial resolution (Eldering et al., 2017). These sensors are considered among the best for XCO2 observation, featuring larger overlapping swaths that cover areas of ~20×80 km² and exhibiting the least retrieval absolute bias, measuring less than 0.4 ppm (Eldering et al., 2019; Taylor et al., 2020). However, the narrow swath of the sensor can only cover limited spatial areas, and caused by the cloud and aerosol contaminations, the data from OCO-2/3 always contain large amount of missing values (Taylor et al., 2016; Crisp et al., 2017). These limitations obstacle the better understanding of the atmosphere-land carbon cycle over large spatial

scale based on satellite observation.

94

95

96

97

98

99

100

101

102

103

104

105

106

107

108

109

110

111

112

113

114

115

116

117

118

119

120

121

122

123

124

125

126

Consequently, several studies have concentrated on generating spatially continuous XCO₂ products based on satellite observations (He et al., 2022; Siabi et al., 2019; Zhang and Liu, 2023). One potential solution is the application of diverse interpolation methods (He et al., 2020; Zeng et al., 2014). However, their results encounter large uncertainty in regions with sparse data coverage, due to the coarse spatial resolution of the original data. In addition, data fusion techniques have gained recognition as an effective method for obtaining full-coverage XCO₂ data (Sheng et al., 2022; He et al., 2022; Siabi et al., 2019; Zhang and Liu, 2023). These techniques can be broadly categorized into two groups. The first category leverages the spatiotemporal correlation inherent in multi-source XCO2 data, fusing them based on this spatiotemporal information (Wang et al., 2023; Sheng et al., 2022). For instance, Wang et al. (2023) introduced a spatiotemporal self-supervised fusion model and generate seamless global XCO₂ data at a spatial resolution of 0.25°. The second category is regression-based methods, which aim to fill the gap by capturing the nonlinear relationship between multi-source XCO₂ measurements and related covariates (He et al., 2022; Siabi et al., 2019; Zhang and Liu, 2023). The specific methodologies include traditional statistical models, geostatistical models and machine learning models. Siabi et al. (2019) employed the Artificial Neural Network (ANN) to establish correlation between XCO₂ and eight environmental variables. Zhang and Liu (2023) utilized the convolution neural networks (CNN) coupled with attention mechanisms to produce full-coverage XCO₂ data across China. Recently, Zhang et al. (2023) developed high spatial resolution global CO₂ concentration data based on deep forest model and multisource satellite products.

Although the development of CO₂ observation satellites and the application of machine learning methods have significantly improved the estimation accuracy of XCO₂, current studies still face several limitations. Firstly, due to the sparse distribution of satellite XCO₂ data, previous studies always relied on assimilation and reanalysis XCO₂ data, such as CAMS XCO₂ with coarse spatial resolution (0.75°). This reliance often results in final products that closely mirror the assimilation and reanalysis results, leading to an oversmoothed distribution that undermines the high-resolution advantages of satellite data. Furthermore, most current studies estimated the spatial distribution of CO₂ primarily based on vegetation and meteorological information, with limited

consideration of the impact of human activities and emissions, despite these have significant influence on atmospheric CO₂ variability. This limitation also led to estimation results that fail to adequately capture the impact of anthropogenic emissions on atmospheric CO₂. In addition, most studies that employ regression models to estimate full-coverage XCO₂ are limited to regional or national scales due to the weak transferability of these models. Only a few studies (Zhang et al., 2023) have explored global-scale CO₂ estimation using machine learning approaches, highlighting the need for further research to enhance model generalizability and scalability. Therefore, we intent to develop the global full-coverage XCO₂ products with the capacity to capture both large-scale patterns and fine spatial details. This development leveraged satellite carbon monitoring, multi-source high spatial resolution auxiliary variables and advanced methods that exhibit spatiotemporal transferability to overcome the aforementioned limitations.

In this study, we leveraged time-series OCO-2/3 XCO₂ data and various related environmental variables from multi-source satellites to generate global full-coverage XCO₂ products. The advanced deep learning method was adopted to model time-series XCO₂ and incorporate terrestrial flux, anthropogenic flux and climatic impacts into the parameterization process. These products are designed to meet the following criteria: (1) high validated accuracy to ensure the reliability of the estimates, (2) high spatial resolution capable of capturing fine-scale variations in CO₂ concentrations, and (3) global full-coverage that overcomes missing values in satellite carbon observations. Our XCO₂ products achieved full global coverage with a spatial resolution of 0.05° and a monthly temporal resolution from 2015 to 2021. We also validated our XCO₂ products against in-situ XCO₂ data and other XCO₂ products. Based on our high-resolution products, we explored the spatial and temporal pattern of atmospheric CO₂ globally and identified regions with intense CO₂ emission. Our findings aim to enhance the understanding of carbon dynamics on a global scale through data reconstruction and analysis.

2. Materials and methods

In this study, we utilized Google Earth Engine (GEE) to integrate OCO-2/3 XCO₂ data and multiple environmental variables as data inputs. In addition, the attention-based Bidirectional Long Short-Term Memory (At-BiLSTM) model was trained for

building the relationship between OCO-2/3 XCO₂ and the related environmental variables. Then, we reconstructed the global monthly XCO₂ and validated the accuracy of the products against TCCON XCO₂ data and the original OCO-2/3 XCO₂ data. We also analyzed the spatial and temporal variation of XCO₂ over the globe and detect the intense CO₂ emission regions. The methodology framework is shown in Fig.1.

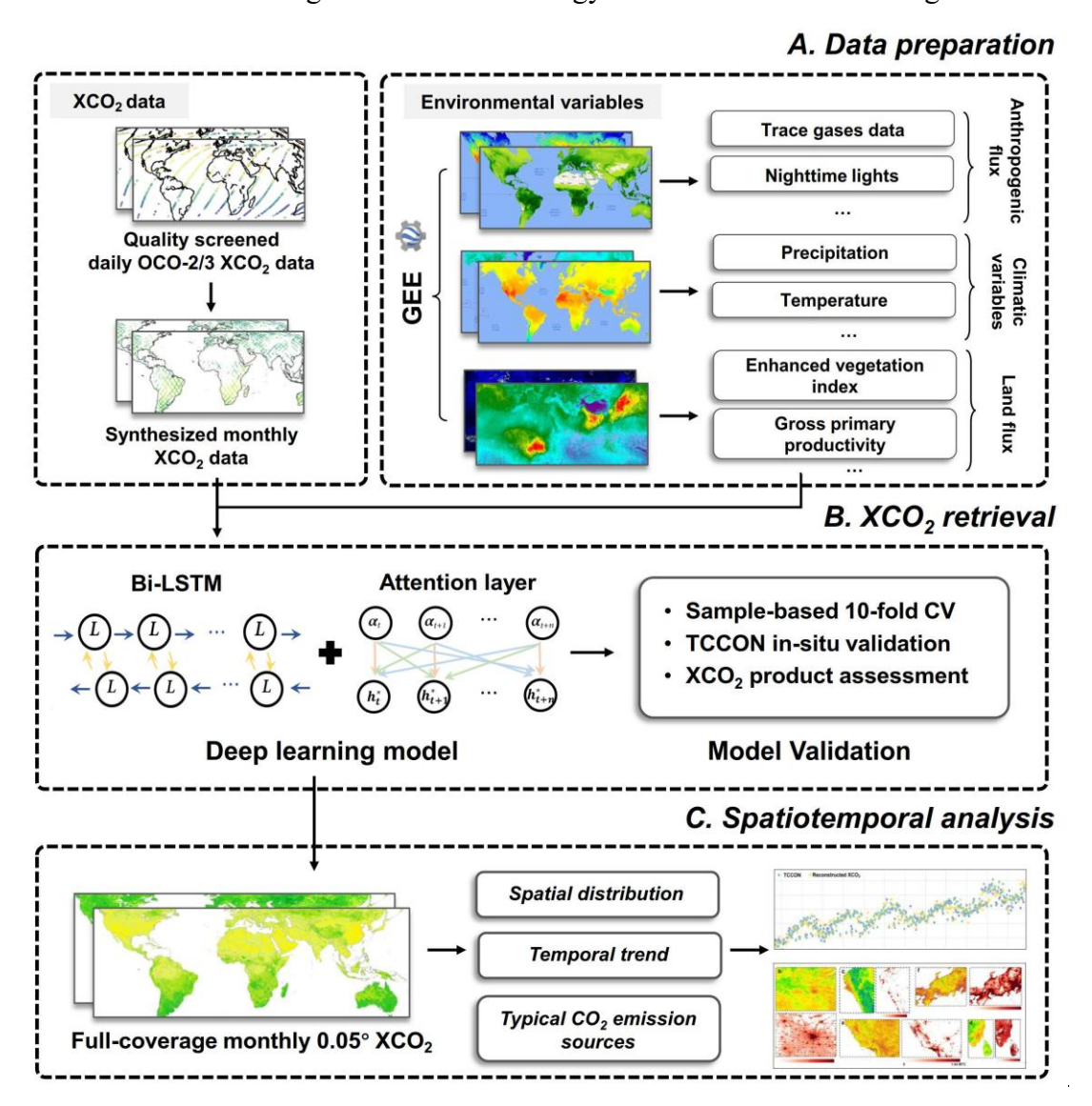


Figure 1. The workflow for mapping and exploring global XCO₂ dynamics and drivers.

2.1 Datasets

2.1.1 OCO XCO₂ data

In this study, we utilized the satellite-based XCO₂ data from OCO-2 and OCO-3, covering the period from December 2014 to December 2021. The OCO-2/3 measure at three near-infrared wavelength bands, that are 0.76 μ m Oxygen A-band, 1.61 μ m weak CO₂, and 2.06 μ m strong CO₂ bands (Crisp et al., 2004). The full physics retrieval

algorithm was used to retrieve the XCO₂ based on the observation of the two satellites (Crisp et al., 2021). Previous studies (Taylor et al., 2023) suggested that the OCO-2 and OCO-3 XCO₂ measurements are in broad consistency and can therefore be used together in scientific analyses. The OCO-3 Level 2 XCO₂ Lite version 10.4r data (OCO3_L2_Lite_FP V10.4r) from 2020 to 2021 and the OCO-2 Level 2 XCO₂ Lite version 11r (OCO2_L2_Lite_FP V11r) from 2015 to 2019 were downloaded from Goddard Earth Sciences Data and Information Services Center (GES DISC, https://disc.gsfc.nasa.gov/). The products were aggregated as a daily file (Fig. 2) with a spatial resolution of 2.25 km × 1.29 km (O'Dell et al., 2018). The XCO₂ data were quality filtered, and only good-quality data (i.e., xco2_quality_flag=0) were considered. To generate the monthly products with a spatial resolution of 0.05° × 0.05°, we converted the daily data to monthly data by averaging the sparse XCO₂ data within a range of 0.05° × 0.05° over one month.

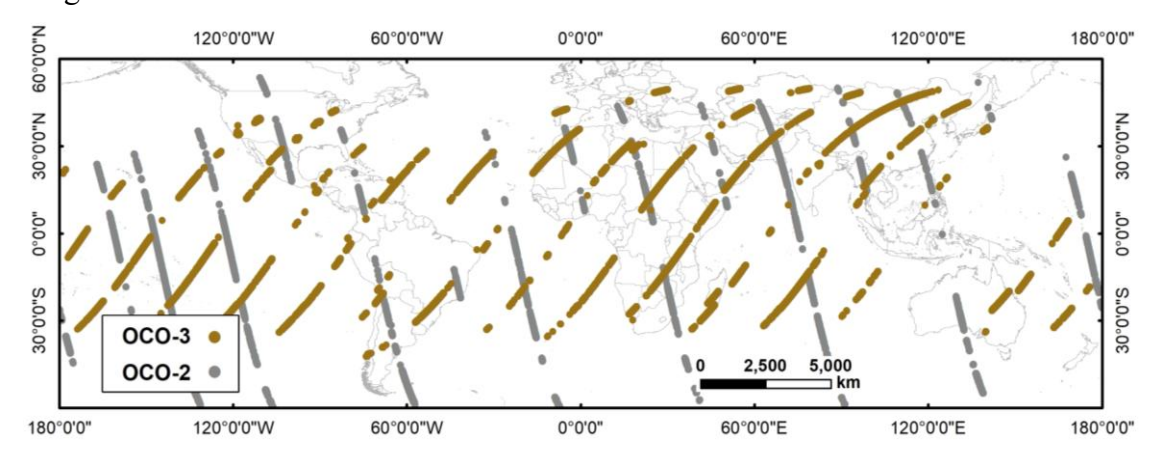
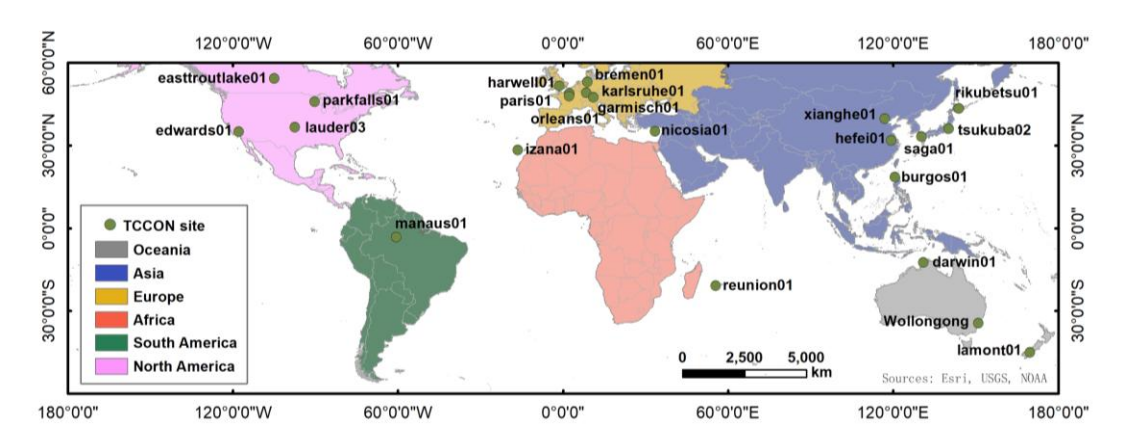


Figure 2. Footprints of OCO-2 and OCO-3 XCO₂ data on 20th January 2018 and 4th December 2021 (with quality filtering) as examples.

2.1.2 TCCON XCO₂ data

The Total Carbon Column Observing Network (TCCON) is a global network for measuring atmospheric CO₂, methane (CH₄), carbon monoxide (CO) and other trace gases in the atmosphere. The XCO₂ data from TCCON were demonstrated to have high accuracy with ~0.2% of XCO₂ (Wunch et al., 2011). Consequently, the data have been used widely for the validation of satellite observations such as OCO-2, OCO-3 and GOSAT (Deng et al., 2016; Wunch et al., 2017). In this research, we used the GGG2014 and GGG2020 datasets from 23 sites (Fig. 3 and Table 1) around the world to validate the reconstructed XCO₂ products.



198199

Figure 3. The locations of the TCCON sites.

200201

Table 1. The information on the TCCON *in situ* stations.

Table 1. The information on the Teeory in still stations.							
ID	Site name	Longitude	Latitude	Start date	End date		
1	saga01 (JP)	130.29	33.24	2011-07-28	2021-06-30		
2	xianghe01 (PRC)	116.96	39.80	2018-06-14	2022-04-09		
3	burgos01 (PH)	120.65	18.53	2017-03-03	2021-08-20		
4	harwell01 (UK)	-1.32	51.57	2021-05-30	2022-05-22		
5	bremen01 (DE)	8.85	53.10	2009-01-06	2021-06-24		
6	tsukuba02 (JP)	140.12	36.05	2014-03-28	2021-03-31		
7	lauder03 (NZ)	-97.49	36.60	2018-10-02	2022-11-14		
8	edwards01 (US)	-117.88	34.96	2013-07-20	2022-12-25		
9	nicosia01 (CY)	33.38	35.14	2019-09-06	2021-06-01		
10	izana01 (ES)	-16.5	28.31	2014-01-02	2022-10-31		
11	orleans01 (FR)	2.11	47.96	2009-09-06	2022-04-24		
12	hefei01 (PRC)	119.17	31.90	2015-11-02	2020-12-31		
13	easttroutlake01 (CA)	-104.99	54.35	2016-10-03	2022-08-13		
14	karlsruhe01 (DE)	8.44	49.10	2014-01-15	2023-01-20		
15	paris01 (FR)	2.36	48.85	2014-09-23	2022-03-28		
16	garmisch01 (DE)	11.06	47.48	2007-07-18	2021-10-18		
17	rikubetsu01 (JP)	143.77	43.46	2014-06-24	2021-06-30		
18	lamont01 (US)	169.68	-45.04	2011-04-16	2022-12-19		
19	reunion01 (RE)	55.48	-20.90	2015-03-01	2020-07-18		
20	darwin01 (AU)	130.93	-12.46	2005-08-28	2020-04-30		
21	Wollongong (AU)	150.88	-34.41	2008-06-26	2020-06-30		
22	Manaus01(BR)	-60.60	-3.21	2014-09-30	2015-07-27		
23	parkfalls01 (US)	-90.27	45.94	2004-06-02	2020-12-29		

JP: Japan, DE: Germany, FI: Finland, FR: French, RE: Réunion Island, AU: Australia, BR: Brazil; US: United States, PRC: People's Republic of China, NO: Norway, CY: Cyprus, NZ: New Zealand, PH: Philippines, UK: United Kingdom, CA: Canada.

2.1.3 Environmental variables

In the selection of environmental variables, our primary focus was on processes within the terrestrial carbon cycle. The carbon cycle on land can be conceptualized as two flux exchange processes influenced by the climatic conditions (Fig. 4). The CO₂ in the atmosphere is fixed by vegetation photosynthesis and the carbon is released back into the atmosphere by respiration and disturbance processes (Beer et al., 2010; Pan et al., 2011). The carbon fluxes through these processes we considered as the land flux. Since Industrial Era, anthropogenic carbon from land use change (e.g., deforestation) and fossil fuels and cement become important parts of atmospheric CO₂ (Friedlingstein et al., 2010), which we considered as the anthropogenic flux. Meanwhile, the two processes are directly or indirectly driven by the climatic features (Sitch et al., 2015; Chen et al., 2021). Consequently, we explored the potential drivers of XCO₂ from the perspective of the carbon cycle at atmosphere-land interface. Multiple satellite products and reanalysis data from three aspects (i.e., land flux, anthropogenic flux and climatic impacts) were selected to consider their various effects on the XCO₂.

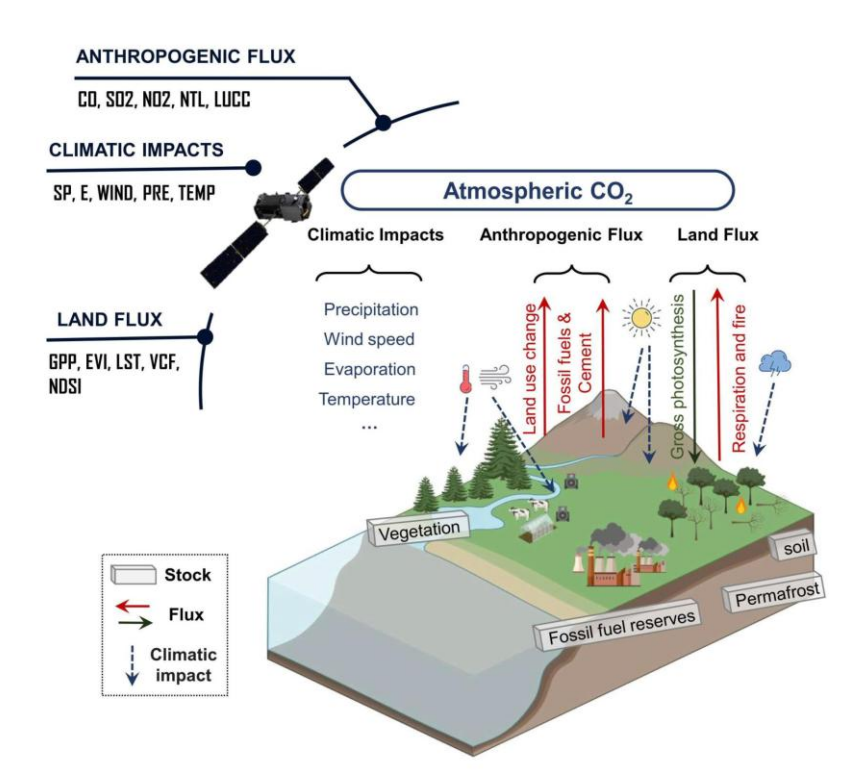


Figure 4. Simplified illustration of the global carbon cycle on land (referring to IPCC

2023). Noting that the carbon cycle in the ocean was not considered in our study and we only focused on the fast exchange fluxes. The slow carbon exchanges (e.g., chemical weathering, volcanic emissions) which are generally assumed as relatively constant over the last few centuries (Sundquist, 1986), were not included here.

The key factors selected related to the land flux included gross primary productivity (GPP), enhanced vegetation index (EVI), land surface temperature (LST), vegetation continuous fields (VCF), and normalized difference snow index (NDSI). These products are all obtained from the Moderate Resolution Imaging Spectroradiometer (MODIS), which has been operated for over 20 years and produced various satellite products with fine spatial resolution and accuracy. The EVI and NDSI were converted to monthly data using the maximum value composite (MVC) method. The GPP and LST were converted to monthly data by the averaging method.

The rising anthropogenic activities have greatly influenced atmospheric CO₂ (Friedlingstein et al., 2022). In this study, five anthropogenic factors, including land use/cover change (LUCC), nighttime lights (NTL), and three trace gases (i.e., sulfur dioxide (SO₂), nitrogen dioxide (NO₂), and carbon monoxide (CO)) were selected. The LUCC was obtained from MODIS MCD12Q1 with a spatial resolution of 500 m. The monthly Suomi National Polar-orbiting Partnership-Visible Infrared Imaging Radiometer Suite (NPP-VIIRS) day/night band (DNB) NTL products (spatial resolution of 15 arc-second, ~500 m) were obtained from the Earth Observation Group (EOG) of the Colorado School of Mines. We also used the SO₂, NO₂ and CO products from the TROPOspheric Monitoring Instrument (TROPOMI) onboard Sentinel-5 Precursor (S5P), a global air monitoring satellite for the Copernicus mission. The data were also converted to the same temporal resolution (i.e., monthly).

The selected climatic factors affecting XCO₂ were surface pressure (SP), 10 m wind speed (WS), precipitation flux (PRE), 2 m air temperature (Temp), and total evaporation (E). These data are from the reanalysis products (Hersbach et al., 2020) developed at the European Center for Medium Weather Forecasting (ECMWF, https://www.ecmwf.int/). The WS is calculated using the products of 10 m wind components of U and V. All data were converted to monthly time-series. The bilinear interpolation approach was employed both to fill gaps in the ancillary data and to convert the data at different spatial resolutions to 0.05° resolution. The data preprocessing was conducted on GEE, R and ArcGIS 10.3. Details of these products

Table 2. Ancillary variables selected in this study.

Variables	Spatial resolution	Temporal resolution	_		
GPP	500 m	8-day MOD17A2H		Land flux-	
EVI	1 km	16-day	MOD13A2	related	
LST	1 km	daily	MOD11A1		
VCF	250 m	annual	MOD44B		
NDSI	500 m	daily	MOD10A1		
LUCC	500 m	annual	MCD12Q1		
NTL	NTL 15 arc-second		VNP46A2	A	
SO_2			OFFL/L3_SO ₂	Anthropogenic	
NO_2	~1 km	daily	OFFL/L3_NO ₂	flux-related	
CO			OFFL/L3_CO		
SP					
E					
Wind-v	10.1	.1.1	EDACI 1	Climatic	
Wind-u	~10 km	monthly	ERA5-Land	impacts	
Pre				_	
Temp					

2.2 Deep learning-based XCO2 reconstruction

Given the complexity temporal dependence and nonlinear relationship between XCO_2 and the environmental variables, we selected the At-BiLSTM model to relate the XCO_2 data with the 16 response variables affecting atmospheric CO_2 , and further reconstruct the XCO_2 data at a fine spatial resolution. The LSTM model is a variant of RNN that excels in modeling temporal sequences and capture long-range dependencies (Hochreiter and Schmidhuber, 1997; Graves et al., 2005), which is essential for understanding the seasonal variations of XCO_2 and dynamic feedbacks between XCO_2 and environmental drivers we selected. Each LSTM cell includes an input gate, a forget gate and an output gate. The forget gate f_t determines which information from the previous time step to forget (Eq. 1):

$$f_t = \sigma(W_f \cdot [h_{t-1}, x_t] + b_f) \tag{1}$$

where σ , W_f , $[h_{t-1}, x_t]$, and b_f denotes the sigmoid activation function, vectors of weights, concatenation of the hidden state at timestep t-1 and the current input, and the bias vector, respectively.

The input gate i_t governs the selective storage of the data in current time step, and the output from forget gate f_t and input gate i_t are combined in the cell state C_t

275 (Eq. 2-3):

$$i_t = \sigma(W_i \cdot [h_{t-1}, x_t] + b_i) \tag{2}$$

$$C_t = f_t \cdot C_{t-1} + i_t \cdot \tanh(W_C \cdot [h_{t-1}, x_t] + b_C)$$
(3)

- where W_i and W_C denote the weight matrix for the input gate and the current cell
- state, respectively; b_i and b_c are the bias vector of the input gate and the current cell
- state, respectively; C_{t-1} and tanh represent the cell state at timestep t-1 and the
- activation function.
- Lastly, the output gate o_t controls the flow of information from the cell state to
- the next time step (Eq. 4).

$$o_t = \sigma(W_0 \cdot [h_{t-1}, x_t] + b_0) \tag{4}$$

- where W_o and b_o denotes the weight matrix and the bias vector of the output gate,
- respectively.
- These gate structures effectively manage the flow of information within the LSTM,
- enabling it to capture the temporal dependencies present in the data (Yuan et al., 2020;
- Wang et al., 2022). Bidirectional LSTM consists of two directional LSTM, in which the
- data flows forward and backward (Graves et al., 2013). The bidirectional structure was
- 288 chosen to enhance the capability of LSTM by allowing the model to consider both past
- and future context in the time series, thereby providing a more comprehensive
- 290 understanding of the underlying temporal dynamics.
- We also defined a multi-dimensional attention layer behind the BiLSTM to focus
- on more critical timesteps and give them higher weights (Bahdanau et al., 2016). This
- 293 is particularly important when dealing with high-dimensional input data comprising
- multi-timestep variables, as it allows the model to assign different weights to different
- 295 timesteps, thereby improving interpretability and predictive performance (Liu and Guo,
- 296 2019; Wang et al., 2024b). Based on this framework, the At-BiLSTM model offers a
- 297 robust and flexible framework for linking XCO₂ with multiple environmental variables
- and reconstructing XCO₂ at a fine spatial resolution with improved accuracy and
- 299 spatiotemporal consistency.
- The At-BiLSTM consists of one input layer, three Bidirectional LSTM (Bi-LSTM)
- 301 layers, one attention layer, one dropout layer to prevent overfitting, and one fully
- 302 connected layer (i.e., dense layer) for the final output. Each Bi-LSTM includes 512
- 303 hidden units and tanh activation in both forward and backward directions. The attention
- 304 mechanism learns a weight distribution over the time dimension using a Dense layer

with softmax activation, then multiplies these weights with the BiLSTM output to emphasize important time steps. The detailed deployment and output are provided in Table 3. The model was implemented using the TensorFlow and Keras deep learning APIs in Python. A time step of 3 was used, and the model was trained for 200 epochs with the mean squared error (MSE) as the loss function. A step-wise decay strategy was applied to the learning rate, where the rate was reduced by a factor of 10 every 50 epochs to enhance training stability and convergence. Prior to training, all input data were normalized using the mean and standard deviation of the dataset.

Table 3. Architecture of the At-BiLSTM model

Layer Name	Layer	Parameters	Output size
Bi-LSTM	Input layer	-	3×16
	Bi-LSTM1	units = 512, activation = 'tanh'	3×1024
	Bi-LSTM2	units = 512, activation = 'tanh'	3×1024
	Bi-LSTM3	units = 512, activation = 'tanh'	3 ×1024
Attention	Attention Permute -		1024×3
	Dense	units = 3, activation = 'softmax'	1024×3
	Permute	-	3 ×1024
	Multiply	-	3 ×1024
Dropout		rate = 0.5	
Full-connect	Dense	units = 1	1

In this study, we adopted the sample-based cross-validation (CV) method to evaluate the model performance and the in-situ validation to assess the accuracy of reconstructed XCO₂ products. We also compared the reconstructed XCO₂ products with the original OCO XCO₂ products and the CAMS-EGG4 GHGs data. Four metrics, including coefficient of determination (R²), root mean squared error (RMSE), mean absolute error (MAE) and mean bias, were calculated as follow, to assess the model performance.

$$R^{2} = 1 - \frac{\sum_{i=1}^{n} (y_{i} - f_{i})^{2}}{\sum_{i=1}^{n} (y_{i} - \bar{y})^{2}}$$
 (5)

$$RMSE = \sqrt{\frac{\sum_{i=1}^{n} (y_i - f_i)^2}{n}}$$
 (6)

$$MAE = \frac{\sum_{i=1}^{n} |(f_i - y_i)|}{n}$$
 (7)

where n is the total number of data samples, and f_i , y_i are the observed results and model-estimated results, respectively.

3. Results

3.1 Validation of the reconstructed XCO₂ product

3.1.1 Model validation results

Given the distinct seasonal variation in XCO₂ concentrations, we conducted the sample-based CV to evaluate the model performance during different seasons (Fig. 5). The model demonstrated high accuracy across all seasons, with R² values exceeding 0.81, MAE less than 0.73 ppm, and RMSE less than 1.09 ppm. The model performed better in spring and summer, as indicated by the densest cluster of points being closest to the 1:1 line. Conversely, the model performed worst in winter, when photosynthesis is weakest, leading to greater estimation deviation. These variations are likely influenced by the ecosystem CO₂ exchange during different seasons. Overall, the model effectively captured the seasonal variation of XCO₂ and provided unbiased XCO₂ estimations.

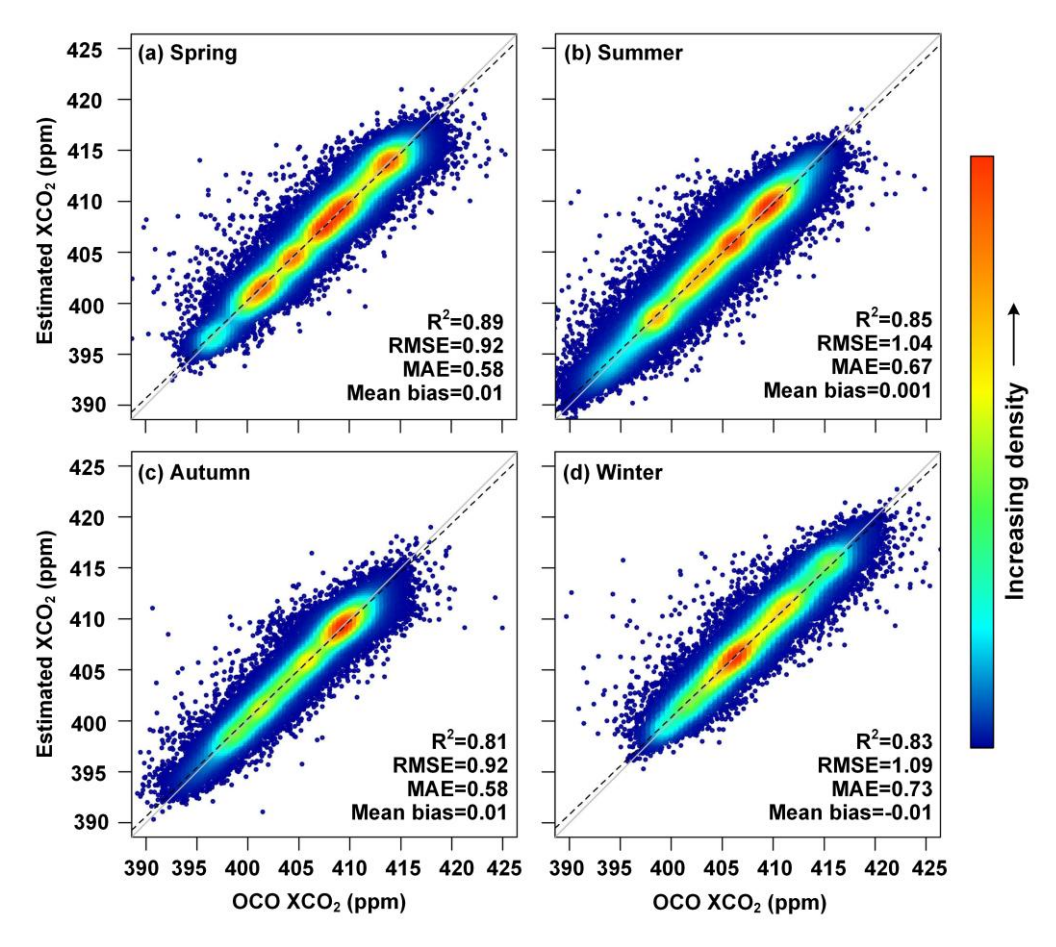


Figure 5. Density scatterplots of sample-based CV results during different seasons. The proportion of the number of points is represented as the color of the points. The black

dashed lines and grey solid lines denote the linear regression fitted lines and the 1:1 line, respectively. The R^2 , RMSE (ppm), MAE (ppm), and mean bias (ppm) are provided.

We further validated the model performance across different continents. Table 4 presents the validation results for six continents. The model performance varied across continents. Notably, the model achieved the highest accuracy in Africa and Europe, with R² of 0.80 and 0.81, and RMSE values of 1.02 and 1.14 ppm, respectively. In contrast, the model demonstrated relatively low accuracy in Oceania and South America, both located in the southern hemisphere. Despite this, the RMSE of the model in these continents were 1.22 and 0.66 ppm, respectively, indicating that the model maintained acceptable estimation accuracy in these regions.

Table 4. Model performance in different continents.

	\mathbb{R}^2	RMSE (ppm)	MAE (ppm)	Mean bias (ppm)
Africa	0.80	1.02	0.70	-0.009
Asia	0.73	1.27	0.85	0.002
Europe	0.81	1.14	0.77	-0.030
North America	0.73	1.26	0.83	-0.020
South America	0.59	1.22	0.86	-0.012
Oceania	0.67	0.66	0.4	0.051

3.1.2 In situ validation results

The TCCON in situ XCO₂ data were adopted for validating the accuracy of the reconstructed XCO₂ over the globe. The validation results for our reconstructed XCO₂ and the origin OCO-2/3 XCO₂ are displayed in Fig. 6. The two XCO₂ data showed similar precision with the R^2 value of 0.91 and 0.92, respectively (Fig. 6c-d). While the reconstructed XCO₂ greatly increases the data coverage with the validation sample increasing from 578 to 1432. Meanwhile, the reconstructed XCO₂ has a smaller RMSE and MAE with values of 1.58 and 1.22 ppm, respectively, compared with the OCO XCO₂. These results indicate that the reconstructed XCO₂ had a closer agreement with TCCON XCO₂. We also displayed the mean bias of OCO and reconstructed XCO₂ in each TCCON site (Fig. 6a-b). As shown in Fig. 6a, the OCO-2/3 observation tend to overestimate the XCO₂, while the reconstructed XCO₂ could amend the underestimation of OCO XCO₂. Over 68% of the validation sites of reconstructed XCO₂ had a mean bias less between \pm 0.4 ppm. Given the orbital constraints of the ISS (Eldering et al.,

2019), OCO-3 measurements were restricted to latitudes below \pm 52°. Consequently, substantial missing values of OCO XCO₂ data were shown around 50°N, introducing a potential bias. In contrast, the reconstructed XCO₂ effectively solves this problem and demonstrates markedly enhanced performance.

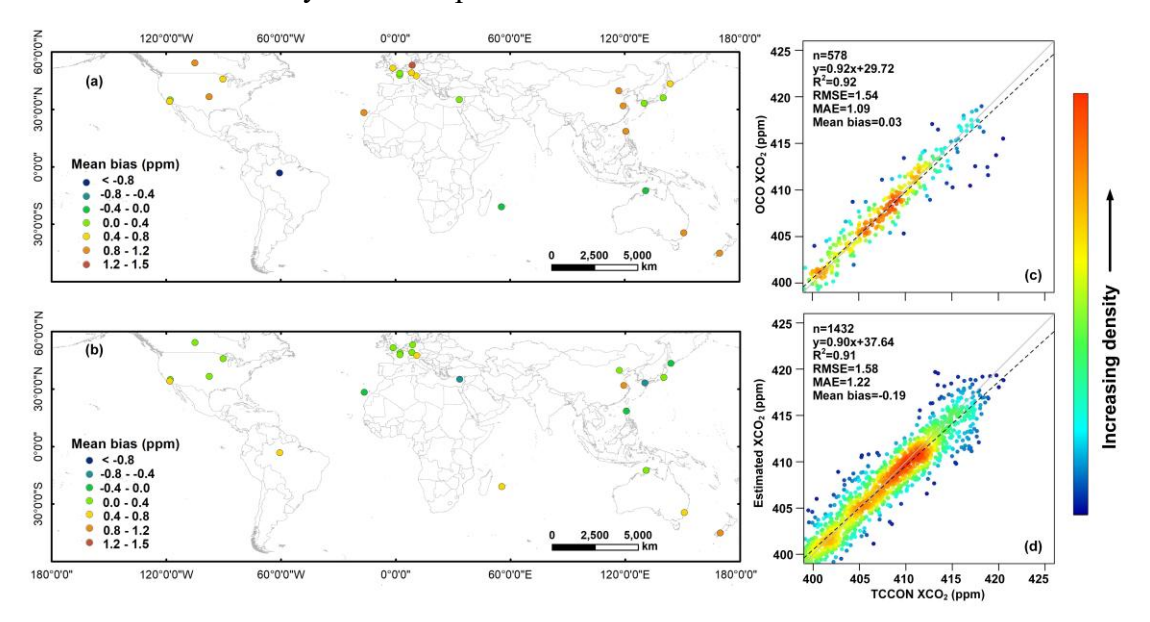


Figure 6. The mean bias of the (a) OCO observed XCO_2 , and (b) reconstructed XCO_2 against global TCCON XCO_2 ; (c) density scatterplots of the validation results for OCO observed XCO_2 , and (d) reconstructed XCO_2 against the TCCON XCO_2 . The proportion of the number of points is represented as the color of the points. The number of samples n, linear regression relation, R^2 , RMSE (ppm), MAE (ppm), and mean bias are provided.

Fig. 7 shows the individual in situ validation results of the reconstructed XCO₂ against TCCON site in different continents (except Antarctica). The sample numbers are varying in different sites due to the observation constraints, while the validation results from all sites showed satisfying performance. The R² for all sites are over 0.88 and the MAE are less than 1.46 ppm. The reconstructed XCO₂ data performs the best in sites lauder03 and karlsruhe01, which located in North America and Europe, respectively. While the reconstructed XCO₂ performed worst in saga01 which located in Asia, potentially due to the high CO₂ concentrations in these regions. Overall, the reconstructed XCO₂ showed high consistency with the in situ XCO₂ observation in different regions over the globe.

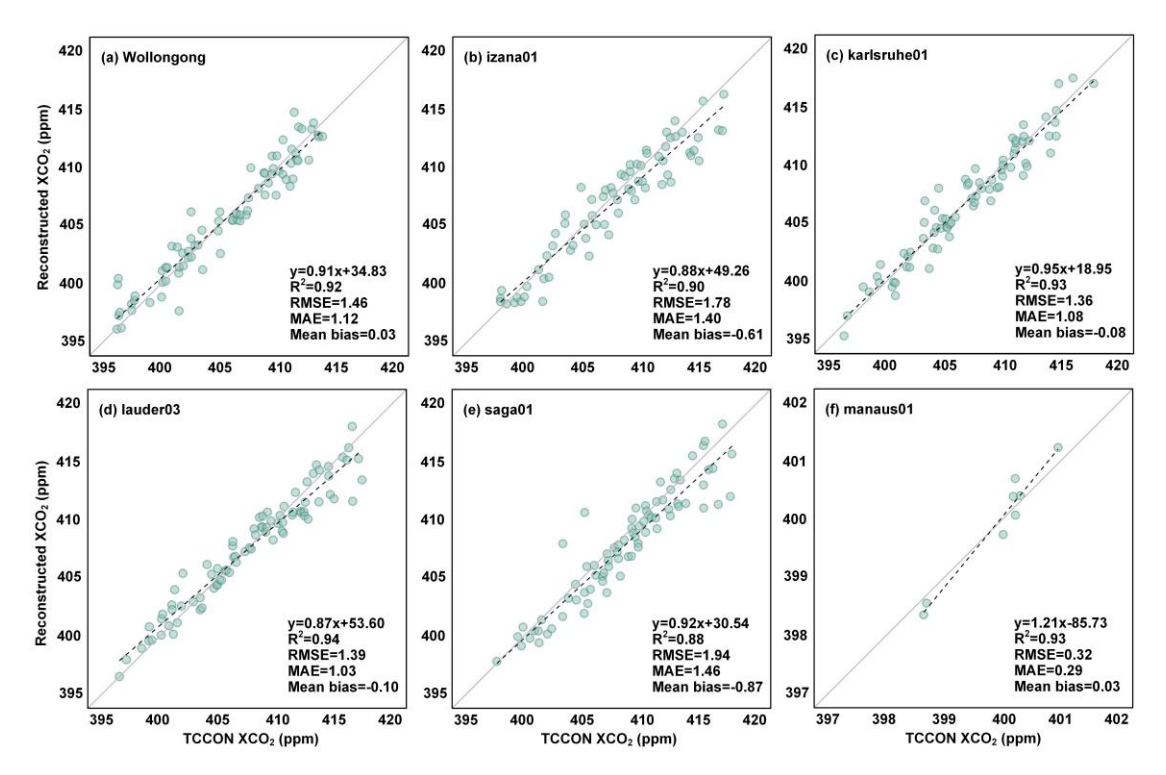


Figure 7. Scatterplots of the TCCON in situ validation results of the reconstructed XCO₂ on different TCCON sites over the globe.

To assess the performance of our reconstructed XCO₂ in temporal analysis, we compared the time series for monthly OCO-2/3, reconstructed and TCCON XCO₂ data from December 2014 to December 2021. As depicted in Fig. 8, the reconstructed XCO₂ exhibits similar temporal patterns compared to the TCCON data, with the mean RMSE and MAE of 1.47 and 1.07 ppm. While the OCO-2/3 XCO₂ exhibits some overestimation for high values and underestimation for low values compared with TCCON data. In contrast, the reconstructed XCO₂ provided more stable estimate results.

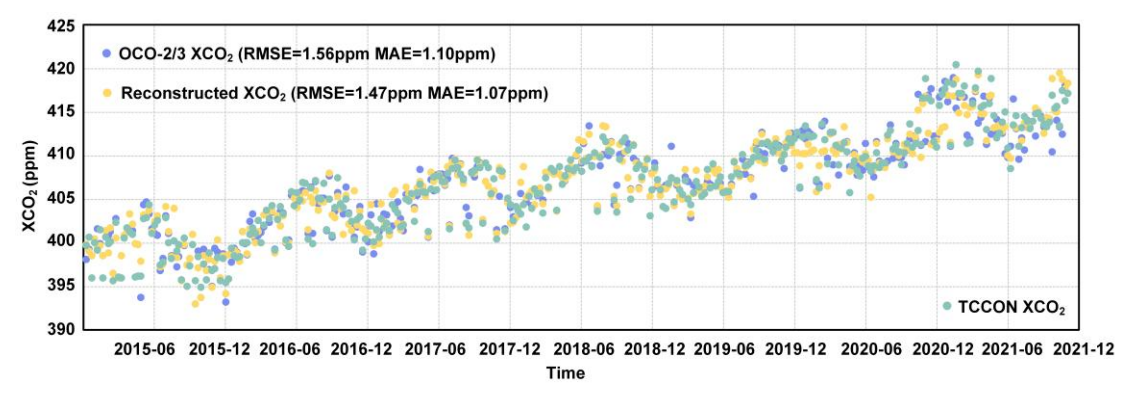


Figure 8. Comparison of the temporal variation of XCO₂ data from OCO-2/3 (blue dots), TCCON (green dots), and the reconstructed products (yellow dots).

3.2 Spatiotemporal pattern of global XCO₂

The global distribution of annual mean XCO₂ concentration from 2015 to 2021 is illustrated in Fig. 9. The results reveal pronounced spatial heterogeneity in XCO₂ concentrations, characterized by a marked hemispheric asymmetry. Specifically, the Northern Hemisphere exhibited systematically elevated XCO₂ levels compared to the Southern Hemisphere, consistent with latitudinal gradients driven by anthropogenic emission patterns and atmospheric transport dynamics. Regionally, North America, East Asia, Central Africa, and northwest of Southern America were identified as persistent hotspots of enhanced XCO₂. The high concentrations of XCO₂ in North America and East Asia stem primarily from the fossil fuel emission from energy production and transportation sectors. Whereas the tropical regions (i.e., Central Africa and South America) are influenced by coupled biomass burning and land-use changes.

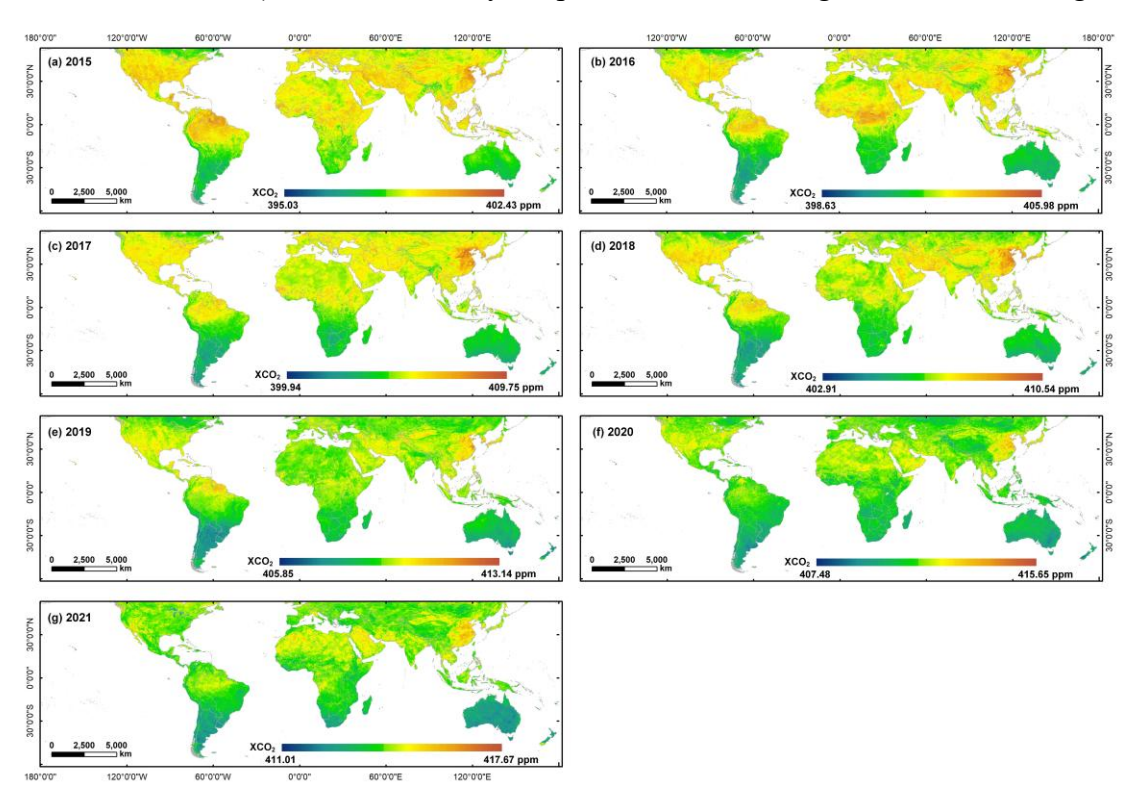


Figure 9. The global spatial distribution of reconstructed annual mean XCO₂ concentration from 2015 to 2021.

We also provided the annual OCO-2 XCO₂ data from 2015 to 2019 and OCO-3 XCO₂ data from 2020 to 2021 in Fig. 10. Spatially, our reconstructed XCO₂ dataset (Fig. 9) demonstrates robust consistency with satellite observations, particularly in midlatitude industrialized regions where both datasets capture emission hotspots. Notably, OCO-3 exhibits denser observational sampling due to its improved spatial coverage and

swath width compared to OCO-2's narrow tracks. However, persistent data gaps remain prevalent in both two satellite products after annual aggregating. These spatial coverage limitations hinder fine-scale global analysis, particularly in assessing localized emission sources and regional scale carbon flux.

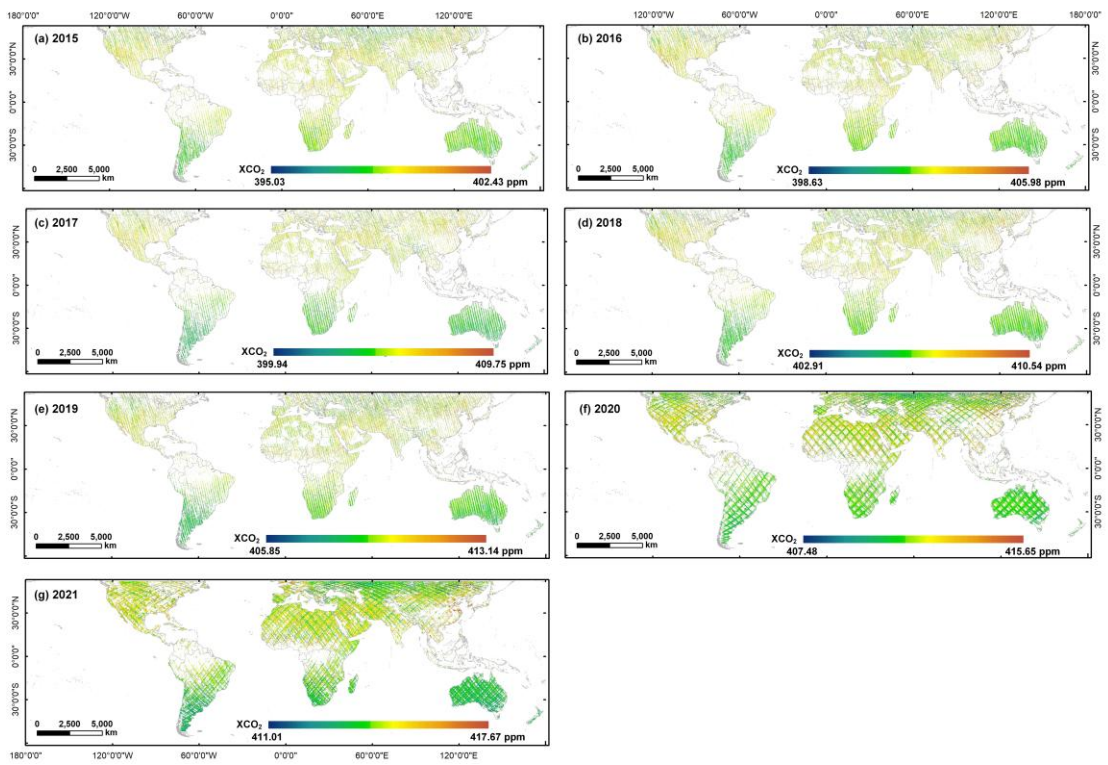


Figure 10. The global spatial distribution of annual mean OCO-2/OCO-3 XCO₂ concentration from 2015 to 2021.

Fig. 11 presents the spatial distribution of the 7-year (2015-2021) averaged XCO₂ concentration and trend over the globe. The average XCO₂ concentration from 2015 to 2021 was 406.90 ± 0.80 ppm worldwide. The highest concentration of XCO₂ mainly occurs in the northern low-to-mid-latitudes (10°N-45°N). More frequent human activities and carbon emissions contributed to higher atmospheric CO₂ concentrations in the Northern Hemisphere. In contrast, the lowest XCO₂ concentration was 404.02 ppm, occurring in the Southern Hemisphere where 81% of the area is ocean. The oceans act as a vital carbon sink and absorb most atmospheric CO₂. For the continent scale, the XCO₂ concentrations showed a slight variation (±1 ppm) between different continents. The largest XCO₂ were mainly occurred in Asia and North America over years, while the lowest XCO₂ concentration all presented in Oceania (Table 4). In terms of temporal trend, the atmospheric CO₂ exhibited a distinct increasing trend over time, with the mean growth rate of 2.32 ppm yr⁻¹. The large growth rate meanly occurs in the northern

low latitudes (0°N-30°N), especially the Middle East and North Africa (growth rate over 2.5 ppm yr⁻¹). Globally, the XCO₂ increased by 14.16 ppm over seven years (Table 4), especially in 2021, with increased values of up to 3 ppm. This result is consistent with the Global Carbon Budget 2022 (Friedlingstein et al., 2022), which reported that the global average atmospheric CO₂ increased sharply in 2021 and reached 414.71 ppm.

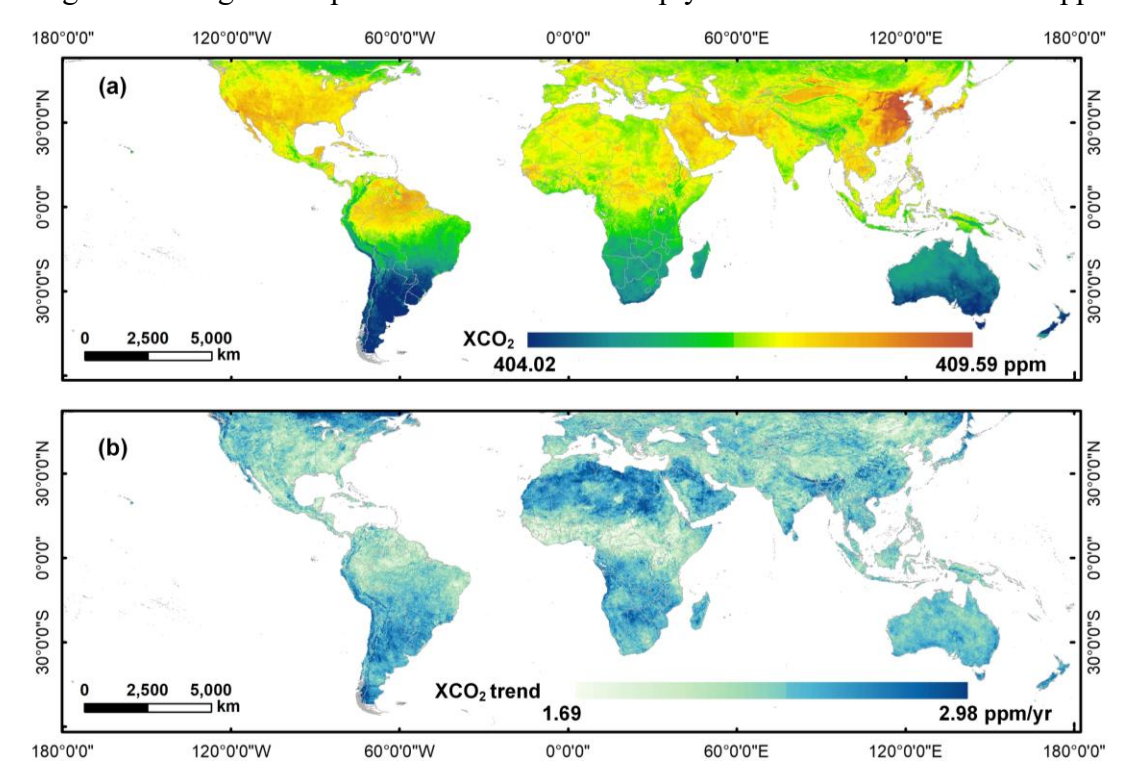


Figure 11. The global spatial distribution of (a) reconstructed 7-year averaged XCO₂ concentration, and (b) its trend from 2015 to 2021 (ppm yr⁻¹ denotes parts per million per year).

Table 4. The reconstructed XCO₂ concentrations at different continents from 2015 to 2021.

Continents	XCO ₂ concentrations (ppm)							
	2015	2016	2017	2018	2019	2020	2021	Increase
Africa	399.26	402.66	404.98	406.71	409.26	411.13	414.11	14.85
Asia	399.57	403.03	405.80	407.37	409.68	411.39	414.38	14.81
Europe	399.55	402.88	405.77	406.96	409.48	411.30	414.17	14.62
North America	399.60	402.95	405.76	407.32	409.70	411.61	414.28	14.68
South America	398.94	401.96	404.27	406.17	408.78	410.47	413.57	14.63
Oceania	398.03	401.04	403.31	405.53	408.13	409.82	412.55	14.52
Global	399.84	401.56	405.16	407.50	409.21	411.07	414.00	14.16

457

458

459

460

461

462

463

464

465

466

467

468

469

470

471

472

473

474

475

3.3 The distribution of XCO₂ anomaly

To better explore the dynamics of global carbon change, we further calculated the XCO₂ anomalies based on the full-coverage XCO₂ products and presented their global distributions from 2015 to 2021 (Fig. 12). The XCO₂ anomalies were calculated by the statistical filtering method, that is, subtracting the global median XCO₂ value from the global XCO₂ distribution (Hakkarainen et al., 2016). The spatial pattern of XCO₂ anomalies were relatively consistent over seven years with no significant variations. From the global perspective, high XCO₂ anomalies mainly occurred in the Northern Hemisphere. East Asia has the largest XCO₂ anomalies with values ranging from 2 to 3 ppm, such as the east part of China. The Middle East, North Africa and the southern part of Northern America also experienced high XCO2 anomalies. Nevertheless, negative XCO₂ anomalies were also identified in the Northern Hemisphere, specifically in regions such as Tibet in China, eastern Canada, and southern Russia. Most negative XCO₂ anomalies were observed in the Southern Hemisphere, which behaves as a carbon sink. However, some positive XCO₂ anomalies are also observed in the tropical regions (e.g., Amazonia), which indicates the Amazonia has changed into a carbon source due to the deforestation and fire occurrence in recent years (Hubau et al., 2020; Gatti et al., 2021).

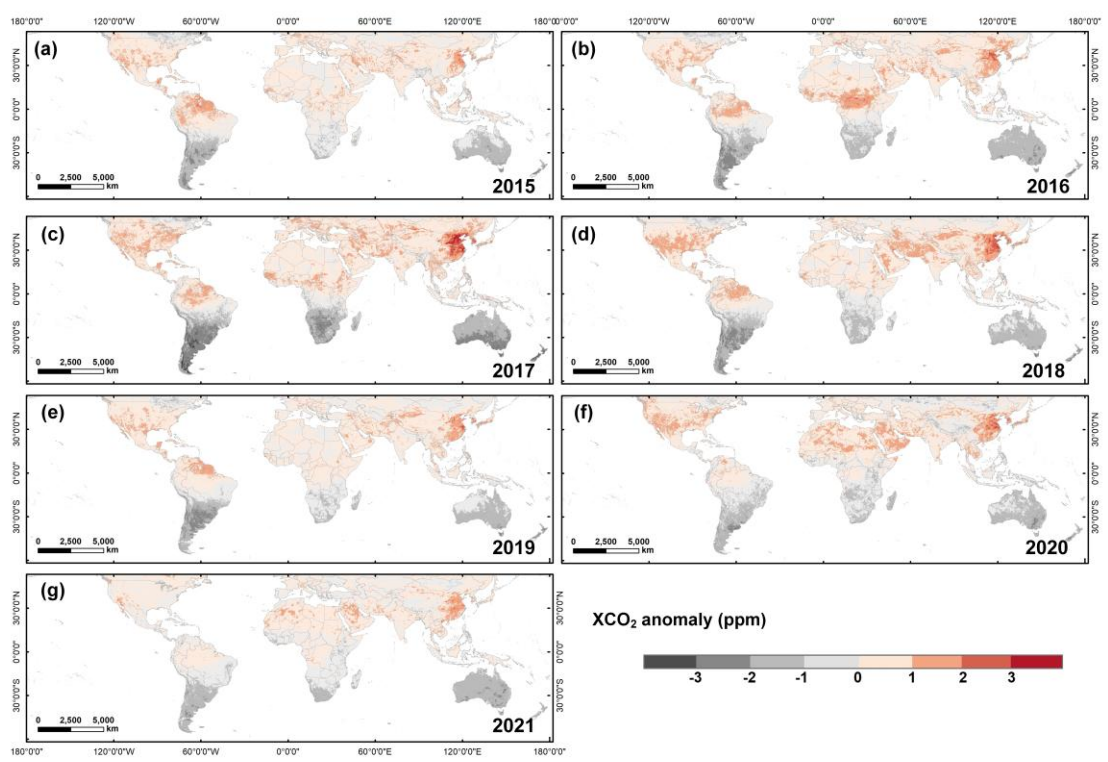


Figure 12. The global spatial distribution of annual XCO₂ anomaly from 2015 to 2021.

Fig. 13 illustrates the detailed spatial distribution of XCO₂ concentrations and anomalies over six regions with high XCO₂ retrievals in 2020. High concentrations of XCO₂ were typically associated with energy-intensive heavy industrial activities, such as Toa Oil Keihin Refinery Factory located in Kawasaki City, Japan (Fig. 13f), and the Shippingport Industrial Park in Pennsylvania, United States (Fig. 13a). Moreover, certain metropolitan transport hubs also exhibited elevated CO₂ anomalies attributable to dense populations and intensive activities. Examples included Shanghai Station in China (Fig.13e) and John F. Kennedy International Airport in New York, USA (Fig. 13b). Attention has also been drawn to natural sources of emissions. Driven by the significant impact of agricultural mechanization and agro-industrial activities on cropland (Lin and Xu, 2018), the XCO₂ anomalies also occurred in the agricultural areas northwestern Jiangsu, China (Fig. 13d). Additionally, we also observed the high XCO₂ anomalies in Amazonia forest in Colombia, which have been suffered from deforestation (Gatti et al., 2023). In conclusion, our products could successfully capture the XCO₂ anomalies from different sources over the globe.

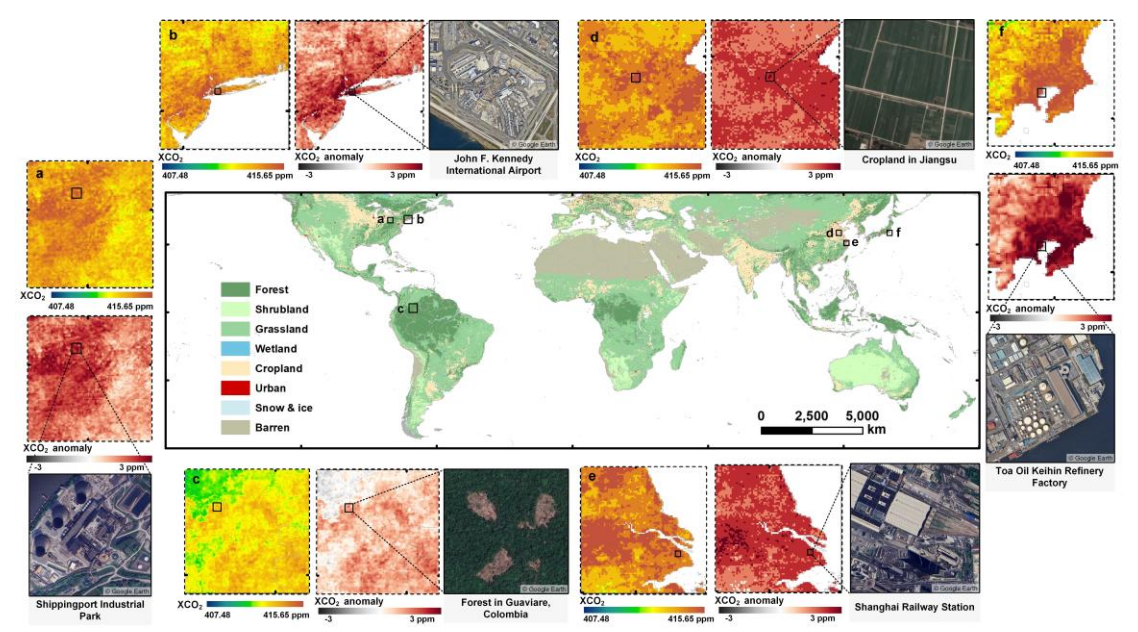


Figure 13. Examples of XCO₂ hotspots in six regions for 2020 detected using the reconstructed products. The subplots present the spatial distribution of XCO₂ concentrations, anomalies (the red panels), and the emission sources (the true color images from Google Earth), respectively. The global map in the middle presents the land use and land cover types over the globe.

4. Discussion

4.1 Comparison with previous studies

To validate the effectiveness of our model and resulting XCO₂ products, we compared our results with current studies which focuses on global XCO₂ reconstruction (Table 5). As for the in-situ validation, most existing studies report high accuracy with almost all R² over 0.9, RMSE less than 2 ppm. Regarding spatial resolution, the various products differ substantially, ranging from 1° down to 0.01°. It should be noted that increasing spatial resolution tends to compromise the accuracy of XCO₂ retrievals. However, our XCO₂ product achieves an optimal balance between spatial detail and measurement precision, exhibiting both high spatial resolution (0.05°) and robust accuracy (R²=0.91, RMSE =1.54 ppm) in comprehensive evaluations.

Table 5. Comparison between current studies focusing on global XCO₂ reconstruction

514

515

516

517

518

519

520

521

522

523

524525

526

527

528

529

530

531

532

533

534

535

536537

Model	Spatial resolution	In-situ validation (with TCCON)			Reference
		R ²	R ² RMSE MAE		-
			(ppm)	(ppm)	
Attentional-based LSTM	0.05°	0.91	1.54	1.22	Our study
Deep forest	0.1°	0.96	1.01	-	Zhang et al. (2023)
S-STDCT	0.25°	0.95	1.18	-	Wang et al. (2023)
Spatiotemporal kriging	1°	0.97	1.13	0.88	Sheng et al. (2022)
MLE & OI	0.5°	0.92	2.62	1.53	Jin et al. (2022)
ERT	0.01°	0.83	1.79	-	Li et al. (2022)

*S-STDCT: Self-supervised spatiotemporal discrete cosine transform; MLE & OI: maximum likelihood estimation method and optimal interpolation; ERT: Extremely randomized trees

To evaluate the advancement of our XCO₂ product, we compared it with original OCO-2 observations and publicly available global XCO₂ datasets (Wang et al., 2023; Sheng et al., 2022; Zhang et al., 2023) across four regions: North America, Europe with northern Africa, Asia, and Oceania (Fig. 14) in January 2015. Despite monthly aggregation, OCO-2 data exhibit persistent spatial discontinuities, limiting the capacity to analyze monthly XCO₂ variability at regional and national scales. Existing XCO₂ products (spatial resolution of 0.25°, 1°, and 0.1°, respectively) broadly reproduce large-scale XCO₂ patterns but fail to resolve fine-scale heterogeneity. In comparison, our reconstructed XCO₂, with the highest spatial resolution, provides a more detailed and accurate representation of the regional XCO₂ patterns. For example, lower XCO₂ concentrations are clearly identified in eastern Canada (The first row of Fig.14) and Papua New Guinea (The fourth row of Fig. 14), regions characterized by dense forest cover. This correspondence highlights the substantial carbon sink potential of these forested areas. Our high-resolution product better identifies the CO₂ heterogeneity associated with different land cover types, whereas the coarse-resolution products smooth these signals. This limitation primarily stems from the neglect of highresolution land cover dynamics and dependence on coarse-resolution assimilated/reanalysis datasets (e.g., CAMS XCO2, CarbonTracker), resulting in oversmoothed spatial patterns that obscure satellite-derived high-resolution signals. Unlike assimilation-dependent approaches, our method avoids XCO₂ reanalysis inputs, preserving satellite-scale fidelity through high-resolution environmental variables modeling while maintaining precision.

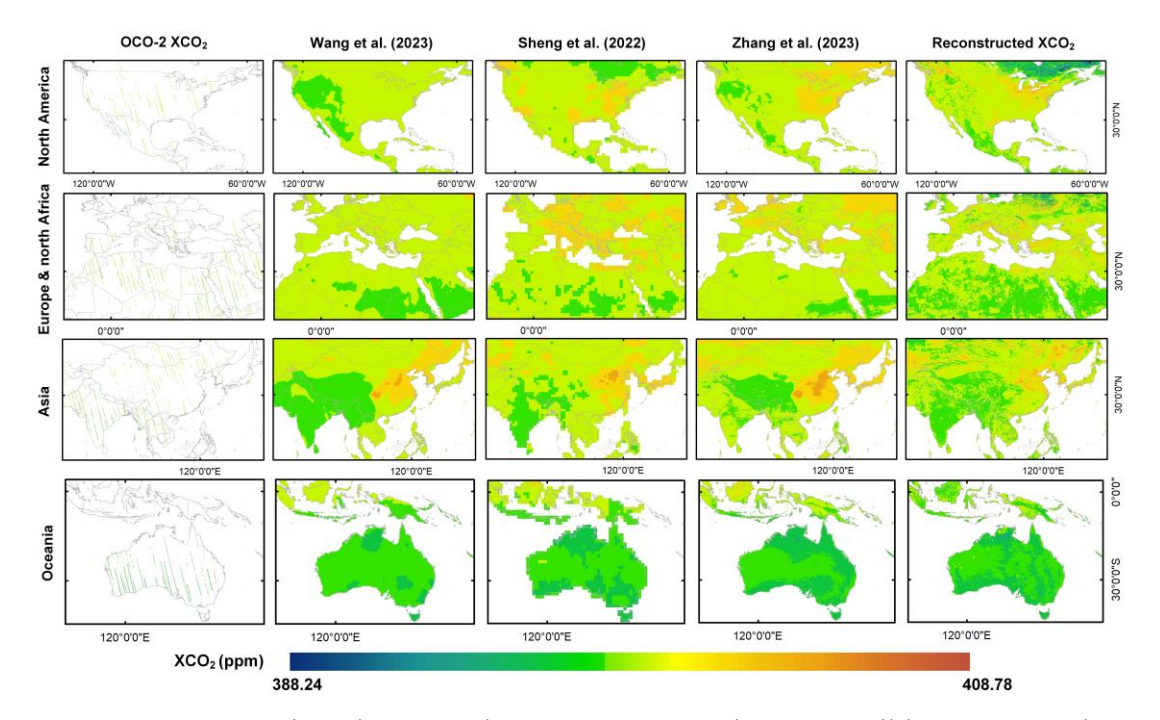


Figure 14. Comparison between the OCO-2 XCO₂ data, accessible XCO₂ products from Wang et al. (2023), Sheng et al. (2022), Zhang et al. (2023), and our reconstructed XCO₂ data in four regions, using the products of January of 2015 as an example.

4.2 Limitations and future improvements

Though our XCO₂ products achieved full spatial coverage and high accuracy, however, there are still several limitations need further improvement. In terms of the satellite data, OCO-2 and OCO-3 provide different spatiotemporal coverages. Analyzing OCO-2 and OCO-3 data simultaneously may introduce several uncertainties due to these differences. However, OCO-3 has a similar sensor and inherits the retrieval algorithms of OCO-2. According to Taylor et al. (2023), the mean differences between OCO-3 and OCO-2 are around 0.2 ppm over land. Therefore, we suppose that the discrepancies between their datasets are minimal, and the combined analysis of data from these two satellites will have a negligible impact on our results.

Additionally, though our model integrates multiple environmental variables associated with surface carbon flux variations, it does not account for vertical atmospheric transport. As XCO₂ represents the column-averaged CO₂ concentration, vertical redistribution of CO₂ through atmospheric transport (e.g., mixing, convection) can alter the relationship between surface carbon fluxes and column concentrations (Shirai et al., 2012). The absence of such vertical transport indicators may reduce the model's accuracy in regions or periods with strong vertical mixing. Future efforts will

incorporate vertical transport-related variables, such as planetary boundary layer height, vertical wind components, and other reanalysis-derived indicators, to better represent the atmospheric processes that influence the column-averaged CO₂ signal.

Moreover, while OCO missions currently provide some of the most accurate carbon satellite-based XCO₂ retrievals, they still encounter some retrieval errors and data gaps driven by algorithmic limitations and variable meteorological conditions. A critical research frontier is the refinement of XCO₂ retrieval algorithms to mitigate systematic biases in high-aerosol-load regions (e.g., industrial regions and biomass-burning plumes). Additionally, next-generation hyperspectral satellites, such as the upcoming CO2M (Copernicus Anthropogenic CO₂ Monitoring Mission) with 2×2 km² resolution and GeoCarb (Geostationary Carbon Observatory) offering hourly monitoring, will enhance spatial-temporal coverage and reduce cloud-induced data gaps (Reuter et al., 2025).

5. Data availability

The XCO₂ dataset produced in this paper is available at https://doi.org/10.5281/zenodo.12706142 (Wang et al., 2024a). It includes monthly global XCO₂ data at 0.05° resolution, covering the period from December 2014 to December 2021. The dataset is archived in netCDF4 format, with units in parts per million (ppm).

6. Conclusion

As a major driver of global warming, the monitoring of CO₂ changes, especially anthropogenic CO₂ emissions, is of critical importance. The launch of carbon satellites offers a significant advancement for CO₂ monitoring. However, the limited spatial coverage of satellite observations constrains the utility of XCO₂ data. While current XCO₂ products exhibit relatively high validation accuracy, their coarse spatial resolution remains inadequate for applications such as regional- or county-level emission monitoring, as well as for the detection and inversion of large emission sources. To address these issues, we reconstructed a global full-coverage XCO₂ product at a fine spatial resolution of 0.05° and temporal resolution of 1 month from 2015 to 2021. The advanced deep learning method was adopted to model time-series XCO₂ and incorporate terrestrial flux, anthropogenic flux and climatic impacts into the

- parameterization process. Through comprehensive evaluations, including cross-validation, in-situ validation, spatial distribution assessment and comparison with other XCO₂ products, our reconstructed XCO₂ products demonstrates significant improvements in both accuracy and spatial resolution. The main conclusions and contributions are as following:
 - (1) The advanced At-BiLSTM model could successfully established the nonlinear relationship between satellite-derived XCO₂ and a set of key environmental variables. And the reconstructed XCO₂ based on our model shows relatively good agreement with TCCON XCO₂, with R², RMSE, and MAE values of 0.91, 1.58 ppm, and 1.22 ppm, respectively.
 - (2) The reconstructed XCO₂ product overcomes the extensive data gaps typically caused by narrow satellite swaths and retrieval interference from clouds and aerosols, achieving complete global coverage. Moreover, relative to existing publicly available full-coverage XCO₂ datasets, our product offers the finest spatial resolution (0.05°) while maintaining comparable accuracy.
 - (3) Our method avoids coarse XCO₂ reanalysis inputs, preserving satellite-scale fidelity through high-resolution environmental variables modeling. Consequently, the products enable enhanced ability in identifying regional- and county-level XCO₂ hotpots, carbon emissions and fragmented carbon sinks, providing a robust basis for targeted global carbon governance policies.

Acknowledgements

590

591

592

593

594

595

596

597

598

599

600

601

602

603

604

605

606

607

608

609

610

620

- The authors would like to express their gratitude to the NASA Goddard Earth Science
- Data and Information Services Center for providing the OCO-2/3 XCO₂ products
- 613 (https://disc.gsfc.nasa.gov/), the NASA Land Processes Distributed Active Archive
- 614 Center (LP DAAC) for providing MODIS data. Our gratitude also goes to the Earth
- Observation Group (EOG) of the Colorado School of Mines for supplying the NPP-
- VIIRS NTL products, the European Space Agency (ESA) for providing the TROPOMI
- data, the Copernicus Climate Data Store for providing the ERA5 reanalysis data and
- 618 CAMS-EGG4 XCO₂ data, and the Total Carbon Column Observing Network for their
- dedication in providing the in situ XCO₂ observations.

Author contributions

ZW developed the overall workflow, processed the data and wrote the manuscript. CZ

- 622 and BH revised the manuscript. KS, YS, and XC compiled the data. SC conceptualized
- 623 and revised the manuscript. PA and QZ supervised this study. All the authors
- 624 contributed to the study.

625 **Competing interests**

626 The contact author has declared that none of the authors has any competing interests.

Financial support 627

- This work was supported by the Key R&D Program of Zhejiang (2022C03078) and 628
- 629 National Natural Science Foundation of China (32241036).

References

- Bahdanau, D., Cho, K., and Bengio, Y.: Neural Machine Translation by Jointly Learning 631 632 to Align and Translate, https://doi.org/10.48550/arXiv.1409.0473, 19 May 2016.
- Beer, C., Reichstein, M., Tomelleri, E., Ciais, P., Jung, M., Carvalhais, N., Rödenbeck, 633
- 634 C., Arain, M. A., Baldocchi, D., Bonan, G. B., Bondeau, A., Cescatti, A., Lasslop,
- G., Lindroth, A., Lomas, M., Luyssaert, S., Margolis, H., Oleson, K. W., Roupsard, 635
- O., Veenendaal, E., Viovy, N., Williams, C., Woodward, F. I., and Papale, D.: 636
- Terrestrial Gross Carbon Dioxide Uptake: Global Distribution and Covariation 637
- with Climate, Science, 329, 834–838, https://doi.org/10.1126/science.1184984, 638 639 2010.
- 640 Bovensmann, H., Burrows, J. P., Buchwitz, M., Frerick, J., Noël, S., Rozanov, V. V.,
- 641 Chance, K. V., and Goede, A. P. H.: SCIAMACHY: Mission Objectives and Measurement Modes, Journal of the Atmospheric Sciences, 56, 127-150, 642
- 643 https://doi.org/10.1175/1520-0469(1999)056<0127:SMOAMM>2.0.CO;2, 1999.
- Buchwitz, M., Reuter, M., Schneising, O., Boesch, H., Guerlet, S., Dils, B., Aben, I., 644
- 645 Armante, R., Bergamaschi, P., Blumenstock, T., Bovensmann, H., Brunner, D.,
- Buchmann, B., Burrows, J. P., Butz, A., Chédin, A., Chevallier, F., Crevoisier, C. 646 647
- D., Deutscher, N. M., Frankenberg, C., Hase, F., Hasekamp, O. P., Heymann, J., 648 Kaminski, T., Laeng, A., Lichtenberg, G., De Mazière, M., Noël, S., Notholt, J.,
- 649 Orphal, J., Popp, C., Parker, R., Scholze, M., Sussmann, R., Stiller, G. P., Warneke,
- T., Zehner, C., Bril, A., Crisp, D., Griffith, D. W. T., Kuze, A., O'Dell, C., 650
- Oshchepkov, S., Sherlock, V., Suto, H., Wennberg, P., Wunch, D., Yokota, T., and 651
- Yoshida, Y.: The Greenhouse Gas Climate Change Initiative (GHG-CCI): 652
- 653 Comparison and quality assessment of near-surface-sensitive satellite-derived
- 654 CO2 and CH4 global data sets, Remote Sensing of Environment, 162, 344–362,
- https://doi.org/10.1016/j.rse.2013.04.024, 2015. 655
- 656 Butz, A., Guerlet, S., Hasekamp, O., Schepers, D., Galli, A., Aben, I., Frankenberg, C.,
- Hartmann, J.-M., Tran, H., Kuze, A., Keppel-Aleks, G., Toon, G., Wunch, D., 657 658
- Wennberg, P., Deutscher, N., Griffith, D., Macatangay, R., Messerschmidt, J.,
- Notholt, J., and Warneke, T.: Toward accurate CO2 and CH4 observations from 659 Geophysical 660 GOSAT, Research Letters, 38,
- https://doi.org/10.1029/2011GL047888, 2011. 661
- 662 Chen, S., Arrouays, D., Leatitia Mulder, V., Poggio, L., Minasny, B., Roudier, P.,
- Libohova, Z., Lagacherie, P., Shi, Z., Hannam, J., Meersmans, J., Richer-de-663

- 664 Forges, A. C., and Walter, C.: Digital mapping of GlobalSoilMap soil properties at 665 broad scale: A review, Geoderma, 409, 115567, https://doi.org/10.1016/j.geoderma.2021.115567, 2022. 666
- 667 Chen, Y., Feng, X., Tian, H., Wu, X., Gao, Z., Feng, Y., Piao, S., Lv, N., Pan, N., and Fu, B.: Accelerated increase in vegetation carbon sequestration in China after 2010: 668 669 A turning point resulting from climate and human interaction, Global Change 670 Biology, 27, 5848–5864, https://doi.org/10.1111/gcb.15854, 2021.
- Crisp, D., Atlas, R. M., Breon, F.-M., Brown, L. R., Burrows, J. P., Ciais, P., Connor, B. 671 672 J., Doney, S. C., Fung, I. Y., Jacob, D. J., Miller, C. E., O'Brien, D., Pawson, S., 673 Randerson, J. T., Rayner, P., Salawitch, R. J., Sander, S. P., Sen, B., Stephens, G. L., Tans, P. P., Toon, G. C., Wennberg, P. O., Wofsy, S. C., Yung, Y. L., Kuang, Z., 674 Chudasama, B., Sprague, G., Weiss, B., Pollock, R., Kenyon, D., and Schroll, S.: 675 676 The Orbiting Carbon Observatory (OCO) mission, Advances in Space Research, 34, 700–709, https://doi.org/10.1016/j.asr.2003.08.062, 2004. 677
- Crisp, D., Pollock, H. R., Rosenberg, R., Chapsky, L., Lee, R. A. M., Oyafuso, F. A., 678 Frankenberg, C., O'Dell, C. W., Bruegge, C. J., Doran, G. B., Eldering, A., Fisher, 679 680 B. M., Fu, D., Gunson, M. R., Mandrake, L., Osterman, G. B., Schwandner, F. M., Sun, K., Taylor, T. E., Wennberg, P. O., and Wunch, D.: The on-orbit performance 681 of the Orbiting Carbon Observatory-2 (OCO-2) instrument and its radiometrically 682 683 calibrated products, Atmospheric Measurement Techniques, 10, 59-81, 684 https://doi.org/10.5194/amt-10-59-2017, 2017.
- Crisp, D., O'Dell, C., Eldering, A., Fisher, B., Oyafuso, F., Payne, V., Drouin, B., Toon, 685 686 G., Laughner, J., Somkuti, P., McGarragh, G., Merrelli, A., Nelson, R., Gunson, M., Frankenberg, C., Osterman, G., Boesch, H., Brown, L., Castano, R., Christi, 687 M., Connor, B., McDuffie, J., Miller, C., Natraj, V., O'Brien, D., Polonski, I., 688 689 Smyth, M., Thompson, D., and Granat, R.: LEVEL 2 FULL PHYSICS ALGORITHM Theoretical Basis Document, 2021. 690

692

693 694

701 702

703

- Deng, F., Jones, D. B. A., O'Dell, C. W., Nassar, R., and Parazoo, N. C.: Combining GOSAT XCO2 observations over land and ocean to improve regional CO2 flux estimates, Journal of Geophysical Research: Atmospheres, 121, 1896-1913, https://doi.org/10.1002/2015JD024157, 2016.
- 695 Eldering, A., Wennberg, P. O., Crisp, D., Schimel, D. S., Gunson, M. R., Chatterjee, A., 696 Liu, J., Schwandner, F. M., Sun, Y., O'Dell, C. W., Frankenberg, C., Taylor, T., 697 Fisher, B., Osterman, G. B., Wunch, D., Hakkarainen, J., Tamminen, J., and Weir, B.: The Orbiting Carbon Observatory-2 early science investigations of regional 698 699 carbon dioxide fluxes, Science, 358, eaam5745, 700 https://doi.org/10.1126/science.aam5745, 2017.
 - Eldering, A., Taylor, T. E., O'Dell, C. W., and Pavlick, R.: The OCO-3 mission: measurement objectives and expected performance based on 1 year of simulated Atmospheric Measurement Techniques, 2341-2370, 12, https://doi.org/10.5194/amt-12-2341-2019, 2019.
- 705 Friedlingstein, P., Houghton, R. A., Marland, G., Hackler, J., Boden, T. A., Conway, T. 706 J., Canadell, J. G., Raupach, M. R., Ciais, P., and Le Quéré, C.: Update on CO₂ 707 emissions, Nature Geosci, 3, 811–812, https://doi.org/10.1038/ngeo1022, 2010.
- 708 Friedlingstein, P., O'Sullivan, M., Jones, M. W., Andrew, R. M., Gregor, L., Hauck, J., Le Quéré, C., Luijkx, I. T., Olsen, A., Peters, G. P., Peters, W., Pongratz, J., 709 710 Schwingshackl, C., Sitch, S., Canadell, J. G., Ciais, P., Jackson, R. B., Alin, S. R.,
- 711 Alkama, R., Arneth, A., Arora, V. K., Bates, N. R., Becker, M., Bellouin, N., Bittig,
- 712 H. C., Bopp, L., Chevallier, F., Chini, L. P., Cronin, M., Evans, W., Falk, S., Feely, 713
 - R. A., Gasser, T., Gehlen, M., Gkritzalis, T., Gloege, L., Grassi, G., Gruber, N.,

- Gürses, Ö., Harris, I., Hefner, M., Houghton, R. A., Hurtt, G. C., Iida, Y., Ilyina,
- 715 T., Jain, A. K., Jersild, A., Kadono, K., Kato, E., Kennedy, D., Klein Goldewijk,
- K., Knauer, J., Korsbakken, J. I., Landschützer, P., Lefèvre, N., Lindsay, K., Liu,
- J., Liu, Z., Marland, G., Mayot, N., McGrath, M. J., Metzl, N., Monacci, N. M.,
- Munro, D. R., Nakaoka, S.-I., Niwa, Y., O'Brien, K., Ono, T., Palmer, P. I., Pan,
- N., Pierrot, D., Pocock, K., Poulter, B., Resplandy, L., Robertson, E., Rödenbeck,
- 720 C., Rodriguez, C., Rosan, T. M., Schwinger, J., Séférian, R., Shutler, J. D.,
- Skjelvan, I., Steinhoff, T., Sun, Q., Sutton, A. J., Sweeney, C., Takao, S., Tanhua,
- 722 T., Tans, P. P., Tian, X., Tian, H., Tilbrook, B., Tsujino, H., Tubiello, F., van der 723 Werf, G. R., Walker, A. P., Wanninkhof, R., Whitehead, C., Willstrand Wranne, A.,
- et al.: Global Carbon Budget 2022, Earth System Science Data, 14, 4811–4900,
- 724 et al.: Global Carbon Budget 2022, Earth System Science Data, 14, 4811–49 725 https://doi.org/10.5194/essd-14-4811-2022, 2022.
- Gatti, L. V., Basso, L. S., Miller, J. B., Gloor, M., Gatti Domingues, L., Cassol, H. L.
- G., Tejada, G., Aragão, L. E. O. C., Nobre, C., Peters, W., Marani, L., Arai, E.,
- Sanches, A. H., Corrêa, S. M., Anderson, L., Von Randow, C., Correia, C. S. C.,
- 729 Crispim, S. P., and Neves, R. A. L.: Amazonia as a carbon source linked to
- 730 deforestation and climate change, Nature, 595, 388–393, 731 https://doi.org/10.1038/s41586-021-03629-6, 2021.
- Gatti, L. V., Cunha, C. L., Marani, L., Cassol, H. L. G., Messias, C. G., Arai, E.,
- Denning, A. S., Soler, L. S., Almeida, C., Setzer, A., Domingues, L. G., Basso, L.
- S., Miller, J. B., Gloor, M., Correia, C. S. C., Tejada, G., Neves, R. A. L., Rajao,
- R., Nunes, F., Filho, B. S. S., Schmitt, J., Nobre, C., Corrêa, S. M., Sanches, A. H.,
- Aragão, L. E. O. C., Anderson, L., Von Randow, C., Crispim, S. P., Silva, F. M.,
- and Machado, G. B. M.: Increased Amazon carbon emissions mainly from decline
- 738 in law enforcement, Nature, 621, 318–323, https://doi.org/10.1038/s41586-023-739 06390-0, 2023.
- Graves, A. and Schmidhuber, J.: Framewise phoneme classification with bidirectional
- LSTM and other neural network architectures, Neural Networks, 18, 602–610,
- 742 https://doi.org/10.1016/j.neunet.2005.06.042, 2005.
- 743 Graves, A., Jaitly, N., and Mohamed, A.: Hybrid speech recognition with Deep
- Hidirectional LSTM, in: 2013 IEEE Workshop on Automatic Speech Recognition
- and Understanding, 2013 IEEE Workshop on Automatic Speech Recognition and
- 746 Understanding, 273–278, https://doi.org/10.1109/ASRU.2013.6707742, 2013.
- Hakkarainen, J., Ialongo, I., and Tamminen, J.: Direct space-based observations of anthropogenic CO₂ emission areas from OCO-2, Geophysical Research Letters, 43, 11,400-11,406, https://doi.org/10.1002/2016GL070885, 2016.
- 750 Hammerling, D. M., Michalak, A. M., and Kawa, S. R.: Mapping of CO2 at high
- spatiotemporal resolution using satellite observations: Global distributions from
- OCO-2, Journal of Geophysical Research: Atmospheres, 117, https://doi.org/10.1029/2011JD017015, 2012.
- 754 He, C., Ji, M., Li, T., Liu, X., Tang, D., Zhang, S., Luo, Y., Grieneisen, M. L., Zhou, Z.,
- and Zhan, Y.: Deriving Full-Coverage and Fine-Scale XCO₂ Across China Based on OCO-2 Satellite Retrievals and CarbonTracker Output, Geophysical Research
- 757 Letters, 49, e2022GL098435, https://doi.org/10.1029/2022GL098435, 2022.
- 758 He, Z., Lei, L., Zhang, Y., Sheng, M., Wu, C., Li, L., Zeng, Z.-C., and Welp, L. R.:
- 759 Spatio-Temporal Mapping of Multi-Satellite Observed Column Atmospheric CO₂ 760 Using Precision-Weighted Kriging Method, Remote Sensing, 12, 576,
- 761 https://doi.org/10.3390/rs12030576, 2020.
- Hersbach, H., Bell, B., Berrisford, P., Hirahara, S., Horányi, A., Muñoz-Sabater, J.,

- 763 Nicolas, J., Peubey, C., Radu, R., Schepers, D., Simmons, A., Soci, C., Abdalla, 764 S., Abellan, X., Balsamo, G., Bechtold, P., Biavati, G., Bidlot, J., Bonavita, M., De 765 Chiara, G., Dahlgren, P., Dee, D., Diamantakis, M., Dragani, R., Flemming, J., 766 Forbes, R., Fuentes, M., Geer, A., Haimberger, L., Healy, S., Hogan, R. J., Hólm, E., Janisková, M., Keeley, S., Laloyaux, P., Lopez, P., Lupu, C., Radnoti, G., de 767 768 Rosnay, P., Rozum, I., Vamborg, F., Villaume, S., and Thépaut, J.-N.: The ERA5 769 global reanalysis, Quarterly Journal of the Royal Meteorological Society, 146, 1999–2049, https://doi.org/10.1002/qj.3803, 2020. 770
- Hochreiter, S. and Schmidhuber, J.: Long Short-Term Memory, Neural Computation, 9, 1735–1780, https://doi.org/10.1162/neco.1997.9.8.1735, 1997.
- 773 Hubau, W., Lewis, S. L., Phillips, O. L., Affum-Baffoe, K., Beeckman, H., Cuni-774 Sanchez, A., Daniels, A. K., Ewango, C. E. N., Fauset, S., Mukinzi, J. M., Sheil, 775 D., Sonké, B., Sullivan, M. J. P., Sunderland, T. C. H., Taedoumg, H., Thomas, S. C., White, L. J. T., Abernethy, K. A., Adu-Bredu, S., Amani, C. A., Baker, T. R., 776 777 Banin, L. F., Baya, F., Begne, S. K., Bennett, A. C., Benedet, F., Bitariho, R., 778 Bocko, Y. E., Boeckx, P., Boundja, P., Brienen, R. J. W., Brncic, T., Chezeaux, E., 779 Chuyong, G. B., Clark, C. J., Collins, M., Comiskey, J. A., Coomes, D. A., Dargie, 780 G. C., de Haulleville, T., Kamdem, M. N. D., Doucet, J.-L., Esquivel-Muelbert, A., 781 Feldpausch, T. R., Fofanah, A., Foli, E. G., Gilpin, M., Gloor, E., Gonmadje, C., 782 Gourlet-Fleury, S., Hall, J. S., Hamilton, A. C., Harris, D. J., Hart, T. B., Hockemba, 783 M. B. N., Hladik, A., Ifo, S. A., Jeffery, K. J., Jucker, T., Yakusu, E. K., Kearsley, 784 E., Kenfack, D., Koch, A., Leal, M. E., Levesley, A., Lindsell, J. A., Lisingo, J., 785 Lopez-Gonzalez, G., Lovett, J. C., Makana, J.-R., Malhi, Y., Marshall, A. R., Martin, J., Martin, E. H., Mbayu, F. M., Medjibe, V. P., Mihindou, V., Mitchard, E. 786 787 T. A., Moore, S., Munishi, P. K. T., Bengone, N. N., Ojo, L., Ondo, F. E., Peh, K. 788 S.-H., Pickavance, G. C., Poulsen, A. D., Poulsen, J. R., Qie, L., Reitsma, J., 789 Rovero, F., Swaine, M. D., Talbot, J., Taplin, J., Taylor, D. M., Thomas, D. W., 790 Toirambe, B., Mukendi, J. T., Tuagben, D., Umunay, P. M., et al.: Asynchronous 791 carbon sink saturation in African and Amazonian tropical forests, Nature, 579, 80-792 87. https://doi.org/10.1038/s41586-020-2035-0, 2020.
- IPCC: Climate Change 2023: Synthesis Report. Contribution of Working Groups I, II
 and III to the Sixth Assessment Report of the Intergovernmental Panel on Climate
 Change [Core Writing Team, H. Lee and J. Romero (eds.)]. IPCC, Geneva,
 Switzerland, pp. 35-115, doi: 10.59327/IPCC/AR6-9789291691647, 2023.
- Jin, C., Xue, Y., Jiang, X., Zhao, L., Yuan, T., Sun, Y., Wu, S., and Wang, X.: A long-term global XCO2 dataset: Ensemble of satellite products, Atmospheric Research, 279, 106385, https://doi.org/10.1016/j.atmosres.2022.106385, 2022.
- Kemp, L., Xu, C., Depledge, J., Ebi, K. L., Gibbins, G., Kohler, T. A., Rockström, J., Scheffer, M., Schellnhuber, H. J., Steffen, W., and Lenton, T. M.: Climate Endgame: Exploring catastrophic climate change scenarios, Proceedings of the National Academy of Sciences, 119, e2108146119, https://doi.org/10.1073/pnas.2108146119, 2022.
- Li, J., Jia, K., Wei, X., Xia, M., Chen, Z., Yao, Y., Zhang, X., Jiang, H., Yuan, B., Tao, G., and Zhao, L.: High-spatiotemporal resolution mapping of spatiotemporally continuous atmospheric CO₂ concentrations over the global continent, International Journal of Applied Earth Observation and Geoinformation, 108, 102743, https://doi.org/10.1016/j.jag.2022.102743, 2022.
- Lin, B. and Xu, B.: Factors affecting CO₂ emissions in China's agriculture sector: A quantile regression, Renewable and Sustainable Energy Reviews, 94, 15–27, https://doi.org/10.1016/j.rser.2018.05.065, 2018.

- Liu, G. and Guo, J.: Bidirectional LSTM with attention mechanism and convolutional layer for text classification, Neurocomputing, 337, 325–338, https://doi.org/10.1016/j.neucom.2019.01.078, 2019.
- O'Dell, C. W., Eldering, A., Wennberg, P. O., Crisp, D., Gunson, M. R., Fisher, B., Frankenberg, C., Kiel, M., Lindqvist, H., Mandrake, L., Merrelli, A., Natraj, V., Nelson, R. R., Osterman, G. B., Payne, V. H., Taylor, T. E., Wunch, D., Drouin, B. J., Oyafuso, F.,...Velazco, V. A.: Improved retrievals of carbon dioxide from Orbiting Carbon Observatory-2 with the version 8 ACOS algorithm. Atmos. Meas. Tech., 11(12), 6539-6576. https://doi.org/10.5194/amt-11-6539-2018, 2018.
- Pan, Y., Birdsey, R. A., Fang, J., Houghton, R., Kauppi, P. E., Kurz, W. A., Phillips, O. L., Shvidenko, A., Lewis, S. L., Canadell, J. G., Ciais, P., Jackson, R. B., Pacala, S. W., McGuire, A. D., Piao, S., Rautiainen, A., Sitch, S., and Hayes, D.: A Large and Persistent Carbon Sink in the World's Forests, Science, 333, 988–993, https://doi.org/10.1126/science.1201609, 2011.
- Petzold, A., Thouret, V., Gerbig, C., Zahn, A., Brenninkmeijer, C. A. M., Gallagher, M.,
 Hermann, M., Pontaud, M., Ziereis, H., Boulanger, D., Marshall, J., Nédélec, P.,
 Smit, H. G. J., Friess, U., Flaud, J.-M., Wahner, A., Cammas, J.-P., and VolzThomas, A.: Global-scale atmosphere monitoring by in-service aircraft current
 achievements and future prospects of the European Research Infrastructure
 IAGOS, Tellus B: Chemical and Physical Meteorology, 68, 28452,
 https://doi.org/10.3402/tellusb.v67.28452, 2016.

836

837

838

839 840

841

842

843844

845

846

- Reuter, M., Hilker, M., Noël, S., Di Noia, A., Weimer, M., Schneising, O., Buchwitz, M., Bovensmann, H., Burrows, J. P., Bösch, H., & Lang, R.: Retrieving the atmospheric concentrations of carbon dioxide and methane from the European Copernicus CO2M satellite mission using artificial neural networks. Atmos. Meas. Tech., 18(1), 241-264. https://doi.org/10.5194/amt-18-241-2025, 2025.
- Sheng, M., Lei ,Liping, Zeng ,Zhao-Cheng, Rao ,Weiqiang, Song ,Hao, and and Wu, C.: Global land 1° mapping dataset of XCO₂ from satellite observations of GOSAT and OCO-2 from 2009 to 2020, Big Earth Data, 7, 170–190, https://doi.org/10.1080/20964471.2022.2033149, 2022.
- Shirai, T., Toshinobu, M., Hidekazu, M., Yousuke, S., Yosuke, N., Shamil, M., & and Higuchi, K.: Relative contribution of transport/surface flux to the seasonal vertical synoptic CO₂ variability in the troposphere over Narita. Tellus B: Chemical and Physical Meteorology, 64(1), 19138. https://doi.org/10.3402/tellusb.v64i0.19138, 2012.
- Siabi, Z., Falahatkar, S., and Alavi, S. J.: Spatial distribution of XCO2 using OCO-2 data in growing seasons, Journal of Environmental Management, 244, 110–118, https://doi.org/10.1016/j.jenvman.2019.05.049, 2019.
- Sitch, S., Friedlingstein, P., Gruber, N., Jones, S. D., Murray-Tortarolo, G., Ahlström,
 A., Doney, S. C., Graven, H., Heinze, C., Huntingford, C., Levis, S., Levy, P. E.,
 Lomas, M., Poulter, B., Viovy, N., Zaehle, S., Zeng, N., Arneth, A., Bonan, G.,
 Bopp, L., Canadell, J. G., Chevallier, F., Ciais, P., Ellis, R., Gloor, M., Peylin, P.,
 Piao, S. L., Le Quéré, C., Smith, B., Zhu, Z., and Myneni, R.: Recent trends and
 drivers of regional sources and sinks of carbon dioxide, Biogeosciences, 12, 653–679, https://doi.org/10.5194/bg-12-653-2015, 2015.
- Solomon, S., Plattner, G.-K., Knutti, R., and Friedlingstein, P.: Irreversible climate change due to carbon dioxide emissions, Proceedings of the National Academy of Sciences, 106, 1704–1709, https://doi.org/10.1073/pnas.0812721106, 2009.
- Sundquist, E. T.: Geologic Analogs: Their Value and Limitations in Carbon Dioxide Research. In J. R. Trabalka & D. E. Reichle (Eds.), The Changing Carbon Cycle:

- 863 A Global Analysis (pp. 371-402). Springer New York. 864 https://doi.org/10.1007/978-1-4757-1915-4 19, 1986.
- Taylor, T. E., O'Dell, C. W., Frankenberg, C., Partain, P. T., Cronk, H. Q., Savtchenko, A., Nelson, R. R., Rosenthal, E. J., Chang, A. Y., Fisher, B., Osterman, G. B., Pollock, R. H., Crisp, D., Eldering, A., and Gunson, M. R.: Orbiting Carbon Observatory-2 (OCO-2) cloud screening algorithms: validation against collocated MODIS and CALIOP data, Atmospheric Measurement Techniques, 9, 973–989, https://doi.org/10.5194/amt-9-973-2016, 2016.
- 871 Taylor, T. E., Eldering, A., Merrelli, A., Kiel, M., Somkuti, P., Cheng, C., Rosenberg, 872 R., Fisher, B., Crisp, D., Basilio, R., Bennett, M., Cervantes, D., Chang, A., Dang, 873 L., Frankenberg, C., Haemmerle, V. R., Keller, G. R., Kurosu, T., Laughner, J. L., 874 Lee, R., Marchetti, Y., Nelson, R. R., O'Dell, C. W., Osterman, G., Pavlick, R., 875 Roehl, C., Schneider, R., Spiers, G., To, C., Wells, C., Wennberg, P. O., Yelamanchili, A., and Yu, S.: OCO-3 early mission operations and initial (vEarly) 876 XCO2 and SIF retrievals, Remote Sensing of Environment, 251, 112032, 877 878 https://doi.org/10.1016/j.rse.2020.112032, 2020.
- 879 Taylor, T. E., O'Dell, C. W., Baker, D., Bruegge, C., Chang, A., Chapsky, L., Chatterjee, A., Cheng, C., Chevallier, F., Crisp, D., Dang, L., Drouin, B., Eldering, A., Feng, 880 L., Fisher, B., Fu, D., Gunson, M., Haemmerle, V., Keller, G. R., Kiel, M., Kuai, 881 882 L., Kurosu, T., Lambert, A., Laughner, J., Lee, R., Liu, J., Mandrake, L., Marchetti, 883 Y., McGarragh, G., Merrelli, A., Nelson, R. R., Osterman, G., Oyafuso, F., Palmer, P. I., Payne, V. H., Rosenberg, R., Somkuti, P., Spiers, G., To, C., Weir, B., 884 885 Wennberg, P. O., Yu, S., and Zong, J.: Evaluating the consistency between OCO-2 and OCO-3 XCO₂ estimates derived from the NASA ACOS version 10 retrieval 886 algorithm, Atmospheric Measurement Techniques, 16, 3173-3209, 887 888 https://doi.org/10.5194/amt-16-3173-2023, 2023.
 - Wang, Z., Hu, B., Huang, B., Ma, Z., Biswas, A., Jiang, Y., and Shi, Z.: Predicting annual PM_{2.5} in mainland China from 2014 to 2020 using multi temporal satellite product: An improved deep learning approach with spatial generalization ability, ISPRS Journal of Photogrammetry and Remote Sensing, 187, 141–158, https://doi.org/10.1016/j.isprsjprs.2022.03.002, 2022.

891

892893

894

895

896

897

898

- Wang, Y., Yuan, Q., Li, T., Yang, Y., Zhou, S., and Zhang, L.: Seamless mapping of long-term (2010–2020) daily global XCO₂ and XCH₄ from the Greenhouse Gases Observing Satellite (GOSAT), Orbiting Carbon Observatory 2 (OCO-2), and CAMS global greenhouse gas reanalysis (CAMS-EGG4) with a spatiotemporally self-supervised fusion method, Earth System Science Data, 15, 3597–3622, https://doi.org/10.5194/essd-15-3597-2023, 2023.
- Wang, Z., Zhang, C., Shi, K., Shangguan, Y., Hu, B., Chen, X., Wei, D., Chen, S., Atkinson, P., and Zhang, Q.: A monthly full-coverage satellite-based global atmospheric CO₂ dataset at 0.05° resolution from 2015 to 2021, https://doi.org/10.5281/zenodo.12706142, 2024a.
- Wang, Z., Zhang, C., Ye, S., Lu, R., Shangguan, Y., Zhou, T., Atkinson, P. M., and Shi,
 Tracking hourly PM_{2.5} using geostationary satellite sensor images and
 multiscale spatiotemporal deep learning, International Journal of Applied Earth
 Observation and Geoinformation, 134, 104145,
 https://doi.org/10.1016/j.jag.2024.104145, 2024b.
- Wunch, D., Toon, G. C., Wennberg, P. O., Wofsy, S. C., Stephens, B. B., Fischer, M. L.,
 Uchino, O., Abshire, J. B., Bernath, P., Biraud, S. C., Blavier, J.-F. L., Boone, C.,
 Bowman, K. P., Browell, E. V., Campos, T., Connor, B. J., Daube, B. C., Deutscher,
 N. M., Diao, M., Elkins, J. W., Gerbig, C., Gottlieb, E., Griffith, D. W. T., Hurst,

D. F., Jiménez, R., Keppel-Aleks, G., Kort, E. A., Macatangay, R., Machida, T., Matsueda, H., Moore, F., Morino, I., Park, S., Robinson, J., Roehl, C. M., Sawa, Y., Sherlock, V., Sweeney, C., Tanaka, T., and Zondlo, M. A.: Calibration of the Total Carbon Column Observing Network using aircraft profile data, Atmospheric Measurement Techniques, 3, 1351–1362, https://doi.org/10.5194/amt-3-1351-

918

934

935

936

937

2010, 2010.

- 919 Wunch, D., Toon, G. C., Blavier, J.-F. L., Washenfelder, R. A., Notholt, J., Connor, B. 920 J., Griffith, D. W. T., Sherlock, V., and Wennberg, P. O.: The Total Carbon Column 921 Observing Network, Philosophical Transactions of the Royal Society A: 922 Mathematical, Physical and Engineering Sciences, 369. 2087-2112, 923 https://doi.org/10.1098/rsta.2010.0240, 2011.
- 924 Wunch, D., Wennberg, P. O., Osterman, G., Fisher, B., Naylor, B., Roehl, C. M., O'Dell, 925 C., Mandrake, L., Viatte, C., Kiel, M., Griffith, D. W. T., Deutscher, N. M., Velazco, V. A., Notholt, J., Warneke, T., Petri, C., De Maziere, M., Sha, M. K., Sussmann, 926 R., Rettinger, M., Pollard, D., Robinson, J., Morino, I., Uchino, O., Hase, F., 927 Blumenstock, T., Feist, D. G., Arnold, S. G., Strong, K., Mendonca, J., Kivi, R., 928 929 Heikkinen, P., Iraci, L., Podolske, J., Hillyard, P. W., Kawakami, S., Dubey, M. K., Parker, H. A., Sepulveda, E., García, O. E., Te, Y., Jeseck, P., Gunson, M. R., Crisp, 930 931 D., and Eldering, A.: Comparisons of the Orbiting Carbon Observatory-2 (OCO-932 2) X_{CO2} measurements with TCCON, Atmospheric Measurement Techniques, 10, 933 2209–2238, https://doi.org/10.5194/amt-10-2209-2017, 2017.
 - Yuan, Q., Shen, H., Li, T., Li, Z., Li, S., Jiang, Y., Xu, H., Tan, W., Yang, Q., Wang, J., Gao, J., and Zhang, L.: Deep learning in environmental remote sensing: Achievements and challenges, Remote Sensing of Environment, 241, 111716, https://doi.org/10.1016/j.rse.2020.111716, 2020.
- Zeng, N., Zhao, F., Collatz, G. J., Kalnay, E., Salawitch, R. J., West, T. O., and Guanter,
 L.: Agricultural Green Revolution as a driver of increasing atmospheric CO₂
 seasonal amplitude, Nature, 515, 394–397, https://doi.org/10.1038/nature13893,
 2014.
- Zhang, L., Li, T., Wu, J., and Yang, H.: Global estimates of gap-free and fine-scale CO₂
 concentrations during 2014–2020 from satellite and reanalysis data, Environment
 International, 178, 108057, https://doi.org/10.1016/j.envint.2023.108057, 2023.
- Zhang, M. and Liu, G.: Mapping contiguous XCO₂ by machine learning and analyzing
 the spatio-temporal variation in China from 2003 to 2019, Science of The Total
 Environment, 858, 159588, https://doi.org/10.1016/j.scitotenv.2022.159588, 2023.